Fatal neuroinvasion of SARS-CoV-2 in K18-hACE2 mice is partially dependent on hACE2 expression

Mariano Carossino[6], Paige Montanaro[1*], Aoife O'Connell[1*], Devin Kenney[1*], Hans Gertje[1], Kyle A. Grosz [1], Susanna A. Kurnick[1], Markus Bosmann[1,4,7], Mohsan Saeed[1,5] Udeni B. R. Balasuriya[6], Florian Douam[1,3$#], and Nicholas A. Crossland[1-2$#]

[1]National Emerging Infectious Diseases Laboratories (NEIDL), Boston University, Boston, MA 02118, USA

[2]Department of Pathology and Laboratory Medicine, Boston University School of Medicine, Boston, MA 02118, USA

[3]Department of Microbiology, Boston University School of Medicine, Boston, MA 02118, USA

[4]Department of Medicine, Pulmonary Center, Boston University School of Medicine, Boston, MA 02118, USA

[5]Department of Biochemistry, Boston University, Boston, MA 02118, USA

[6]Louisiana Animal Disease Diagnostic Laboratory (LADDL) and Department of Pathobiological Sciences, School of Veterinary Medicine, Louisiana State University, Baton Rouge, LA, USA

[7] Center for Thrombosis and Hemostasis, University Medical Center of the Johannes Gutenberg-University, Mainz, Germany

*, $ These authors contributed equally to the work.

Co-corresponding author's contact information: Florian Douam, PhD, fdouam@bu.edu, (617)-358-9174; Nicholas Crossland, DVM, ncrossla@bu.edu, (617)-358-9285.

Running Title: Spatiotemporal analysis of SARS-CoV-2 and *hACE2* in K18-hACE2 mice

Keywords: Translational animal model, comparative pathology, immunohistochemistry, *in situ* hybridization, viral pathogenesis

SUMMARY

COVID-19 is a respiratory disease caused by SARS-CoV-2, a betacoronavirus. Here, we show that in a widely used transgenic mouse model of COVID-19, lethality is invariably associated with viral neuroinvasion and the ensuing neuronal disease, while lung inflammation remains moderate.

ABSTRACT

Animal models recapitulating the distinctive features of severe COVID-19 are critical to enhance our understanding of SARS-CoV-2 pathogenesis. Transgenic mice expressing human angiotensin-converting enzyme 2 (hACE2) under the cytokeratin 18 promoter (K18-hACE2) represent a lethal model of SARS-CoV-2 infection. However, the cause(s) and mechanisms of lethality in this mouse model remain unclear. Here, we evaluated the spatiotemporal dynamics of SARS-CoV-2 infection for up to 14 days post-infection. Despite infection and moderate inflammation in the lungs, lethality was invariably associated with viral neuroinvasion and neuronal damage (including spinal motor neurons). Neuroinvasion occurred following virus transport through the olfactory neuroepithelium in a manner that was only partially dependent on hACE2. Interestingly, SARS-CoV-2 tropism was overall neither widespread among nor restricted to only ACE2-expressing cells. Although our work incites caution in the utility of the K18-hACE2 model to study global aspects of SARS-CoV-2 pathogenesis, it underscores this model as a unique platform for exploring the mechanisms of SARS-CoV-2 neuropathogenesis.

INTRODUCTION

The world is experiencing the devastating effects of the Coronavirus Disease 2019 (COVID-19) pandemic, a highly contagious viral respiratory disease caused by the newly emerged betacoronavirus, Severe Acute Respiratory Syndrome Coronavirus-2 (SARS-CoV-2) (Andersen et al., 2020; Coronaviridae Study Group of the International Committee on Taxonomy of, 2020; Wang et al., 2020a). The initial index case was reported at a seafood market in Wuhan, Hubei Province, China in late 2019 (Andersen et al., 2020). While still under investigation, it has been postulated that the progenitor of SARS-CoV-2 may have originated from horseshoe bats (*Rhinolophus affinis*) or Malayan pangolins (*Manis javanica*) that, following spill over into humans, acquired the genomic features leading to adaptation and human-to-human transmission (Andersen et al., 2020). SARS-CoV-2 has a high transmissibility rate and, to date, it has infected nearly 84.5 million people with over 1.8 million fatalities (Johns Hopkins University & Medicine, 2020). COVID-19 causes respiratory disease of variable severity, ranging from mild to severe, with the development of acute respiratory distress syndrome (ARDS) requiring intensive care and mechanical ventilation (Goyal et al., 2020; Tenforde et al., 2020; Wang et al., 2020a; Wang et al., 2020b). Numerous comorbidities including hypertension, obesity and diabetes, among others, are affiliated with an increased risk of developing severe COVID-19 (Goyal et al., 2020; Simonnet et al., 2020; Tartof et al., 2020; Team, 2020; Tenforde et al., 2020). Furthermore, a proportion of infected patients develop poorly understood neurological signs and/or symptoms mostly associated with the loss of smell and taste (anosmia and ageusia), headache, dizziness, encephalopathy (delirium), and ischemic injury (stroke), among other uncommon symptoms (DosSantos et al., 2020; Eliezer et al., 2020; Ellul et al., 2020;

Goyal et al., 2020; Lee et al., 2020; Liu et al., 2020; Solomon et al., 2020; Walker et al., 2020; Wang et al., 2020b). Recently, SARS-CoV-2 RNA and antigen has been reported in the brain of COVID-19 patients and the olfactory mucosa postulated as a port of entry (Meinhardt et al., 2020). COVID-19 has severely challenged health care systems around the globe, with the urgent need for medical countermeasures including the development of efficacious vaccines and therapeutics.

Animal models permissive to SARS-CoV-2 that could serve as suitable models to understand the pathogenesis of COVID-19 and as preclinical models for the evaluation of vaccine and therapeutic targets are critically needed (Johansen et al., 2020; McNamara et al., 2020; Munoz-Fontela et al., 2020). While various animal models (mice, hamsters, non-human primates, ferrets, minks, dogs, and cats) have been evaluated to date (Gaudreault et al., 2020; Imai et al., 2020; Meekins et al., 2020; Munoz-Fontela et al., 2020; Rockx et al., 2020; Shi et al., 2020; Shuai et al., 2020; Sia et al., 2020; Winkler et al., 2020), none faithfully recapitulates all of the pathological features of COVID-19. The main limitation in the development of suitable murine models of COVID-19 is related to the virus entry mechanism: SARS-CoV-2 binds to target cells via interaction between the viral spike protein (S) and the host angiotensin-converting enzyme 2 (ACE2), considered to be the major host entry receptor (Hoffmann et al., 2020). The low binding affinity between the S protein and murine ACE2 (mACE2) renders conventional mouse strains naturally resistant to infection, posing a challenge in the development of murine models of COVID-19 (Conceicao et al., 2020; Damas et al., 2020; Dinnon et al., 2020). These difficulties have been circumvented by the development of transgenic murine models that express human ACE2 (hACE2) under

different promoters including cytomegalovirus (CMV), hepatocyte nuclear factor-3/forkhead homologue 4 (HFH4), and cytokeratin 18 (K18) (Jiang et al., 2020; McCray et al., 2007; Rathnasinghe et al., 2020; Winkler et al., 2020; Zheng et al., 2020). The transgenic murine model expressing hACE2 under a K18 promoter (namely K18-hACE2) was developed by McCray et al in 2007 to study SARS-CoV (McCray et al., 2007), which shares the same host receptor as SARS-CoV-2 (Li et al., 2003).

SARS-CoV-2 infection of K18-hACE2 mice results in up to 100% lethality similar to what has been reported for SARS-CoV (McCray et al., 2007; Winkler et al., 2020; Zheng et al., 2020). Lethality was reported to be associated with lung inflammation and impaired respiratory function, suggesting that this model can recapitulate features of the respiratory disease observed in severe cases of COVID-19 (Rathnasinghe et al., 2020; Winkler et al., 2020; Zheng et al., 2020). While several studies have reported SARS-CoV-2 neuroinvasion and neurological signs of disease in infected K18-hACE2 mice (Golden et al., 2020; Zheng et al., 2020), the contribution of CNS disease in the lethality of the model and the mechanism by which neuroinvasion occurs, remain unclear.

Under K18 regulation, the expression of hACE2 is reported to be limited mainly to airway epithelial cells and enterocytes lining the colonic mucosa, to a lower degree within kidney, liver, spleen and small intestine, and a minor level of expression in the brain (McCray et al., 2007). However, the cellular distribution of ACE2, and particularly hACE2, in tissues of K18-hACE2 mice remains largely undetermined. We hypothesized that the nature, severity, and outcome of disease in K18-hACE2 mouse model is not solely dictated by the expression and tissue distribution of hACE2 and that increased

lethality in this model is related to neuroinvasion. To investigate this hypothesis, we undertook a comprehensive spatiotemporal analysis of histologic changes, cellular distribution and abundance of viral antigen and RNA along with detailed analysis of the distribution of hACE2 and its correlation with SARS-CoV-2 tropism.

Although SARS-CoV-2 antigen and RNA could be detected in ACE2-expressing cells such as olfactory neuroepithelium (ONE) and alveolar type 2 (AT2) cells, we found that SARS-CoV-2 primarily infected neurons and alveolar type 1 (AT1) cells lacking ACE2 expression. The lethality of the K18-hACE2 model was entirely due to viral neuroinvasion, which occurred through the olfactory neuroepithelium. This process was accompanied by clinically detectable neurological manifestations, and was partially driven by ACE2-independent mechanisms. Altogether, this study expands the current knowledge on the K18-hACE2 murine model to study COVID-19. Our findings will help refine its utilization for providing a relevant understanding of the molecular mechanisms driving neuropathogenesis and pulmonary pathology.

RESULTS

SARS-CoV-2 is invariably fatal in infected K18-hACE2 mice with evidence of neuroinvasion. K18-hACE2 mice inoculated intranasally with SARS-CoV-2 ($1x10^6$ plaque-forming units [PFU]; n=47 [n=25 male and n=12 female) began losing weight as early as 2-3 days post-infection (dpi) irrespective of sex, with maximum weight loss occurring at 7 dpi (17.7% ± 7.8% in male mice, 21.8% ± 3.1% in female, and combined 18.9% ± 6.9%; Figure 1A). Trends in weight loss were associated with an increase in

clinical scores and a decline in core body temperature, both of which became most pronounced near the time of death (Figure 1B-C). SARS-CoV-2-infected K18-hACE2 mice exhibited neurological signs by 6-7 dpi, characterized by tremors, proprioceptive defects, abnormal gait and imbalance. The majority of the animals were either euthanized at this time or were found dead in their cage (93%; 28/30 [Figure 1D]). At the time of death (7-10 dpi), the median clinical score was 3 (interquartile range = 2) and the mean body temperature 30.6 ± 3.7 °C. Two male mice survived to the end of the 14-day observation period. One of these animals had a maximum clinical score of 3/5 at 10 dpi and lost a maximum of 6% body weight, while the other displayed no clinical signs or appreciable weight loss over the observation period. Furthermore, neither of the two male survivors were hypothermic at any point in time, a feature that was consistently observed in animals that succumbed to disease.

When compared with C57BL/6J mice, which were concomitantly infected with SARS-CoV-2, the K18-hACE2 mice had several dark red, slightly depressed foci of variable size (2-3 mm), scattered throughout the lung lobes at 2 and 4 dpi. By 7 dpi, these foci grew into large coalescing, dark red depressions encompassing around 30% of the pulmonary parenchyma, leading to the abnormal pulmonary buoyancy (i.e. tissues sank when placed in formalin). Additionally, the mice euthanized due to clinical deterioration frequently had a markedly dilated urinary bladder filled with concentrated urine. The mice euthanized at 14 dpi (n=2) had sporadic dark red pinpoint foci in the pulmonary parenchyma.

Lethality was associated with significant viral load in the lung and brain of the K18-hACE2 mice (Figure 1E), as previously reported (Golden et al., 2020; Rathnasinghe et

al., 2020; Winkler et al., 2020; Zheng et al., 2020). In the lung, viral RNA was detectable at the earliest experimental timepoint (2 dpi), with a mean of $6.42x10^7$ RNA copies/mg, peaked at 4 dpi (mean of $5.8x10^8$ RNA copies/mg) and remained high at 7 dpi (mean of $3.71x10^7$ RNA copies/mg). In contrast, viral RNA in the brain was low at 2 dpi (mean of $2.46x10^5$ RNA copies/mg) but dramatically increased at 7 dpi (4-log increase) representing the highest viral RNA load during the course of the study, with a mean of $1.27x10^9$ RNA copies/mg. A small amount of viral RNA was detected in the serum ($<10^6$ RNA copies/ml). However, incubation of SARS-CoV-2 permissive cell lines (i.e. Vero E6 cells) with serum samples did not result in any detectable productive infection *in vitro*, confirming that K18-hACE2 are not viremic during infection and that small amounts of naked viral RNA might be circulating in the bloodstream following release from infected tissues (data not shown). Altogether, these data illustrate that lethality was associated with increasing viral load in the brain until time of death, in contrast to lung viral load.

Transient SARS-CoV-2 infection in the nasal cavity of K18-hACE2 mice. We next performed detailed histologic analysis of various tissues to uncover the mechanism of lethality in K18-hACE2 mice. For this, we first focused on the spatial and temporal dynamics of SARS-CoV-2 infection in the upper respiratory tract and analyzed the anterior/rostral nasal cavity and olfactory neuroepithelium for disease-associated lesions. To do so, we performed a thorough sequential histologic analysis combined with immunohistochemistry (IHC) and RNAscope® *in situ* hybridization (ISH) in order to

189 determine the cellular localization and abundance of SARS-CoV-2 antigen and RNA,
190 using an anti-spike monoclonal antibody and an S-specific RNA probe, respectively.
191 At 2 dpi, the anterior/rostral nasal cavity was characterized by mild, multifocal
192 neutrophilic inflammation (rhinitis) in all infected K18-hACE2 mice. In the rostral and
193 intermediate turbinates, histologic changes were characterized by segmental
194 degeneration and necrosis of the lining transitional and respiratory epithelium, with cell
195 rounding, loss of cilia and sloughing, along with scattered intracytoplasmic SARS-CoV-2
196 antigen and RNA (Figure 2). Nasal passages were partially filled with small amounts of
197 cellular debris, degenerate neutrophils and small numbers of erythrocytes. The lamina
198 propria underlying affected areas was infiltrated by low to mild numbers of neutrophils
199 and fewer lymphocytes (Figure 2). SARS-CoV-2 antigen and RNA were detected within
200 the epithelium lining the mucosa of rostral and intermediate turbinates. At 4 dpi,
201 epithelial degeneration and necrosis in the rostral and intermediate turbinates were no
202 longer observed, and histologic changes were consistent with mild, multifocal
203 lymphocytic rhinitis with rare clusters of few neutrophils within the lamina propria (Figure
204 2). Nasal passages were clear of exudate. The abundance of SARS-CoV-2 antigen and
205 RNA decreased, and was mostly restricted to rare positive cells in the respiratory
206 epithelium (Figure 2, Table 1 and Table S1). By 7 dpi, the nasal passages (including the
207 ONE) were histologically within normal limits and no SARS-CoV-2 antigen or RNA were
208 detectable in the rostral and intermediate turbinates (Figure S1).

209 The ONE was histologically unremarkable at all timepoints despite the variable amounts
210 of viral antigen and RNA detected during the course of the study. At 2 dpi, multifocal
211 clusters of cells within the ONE contained abundant SARS-CoV-2 antigen and RNA

(Figure 2, Table 1 and Table S1), becoming gradually more rare at 4 and 7 dpi. No SARS-CoV-2 antigen or RNA were detected in the ONE by 14 dpi (Table 1, Table S1, and Figure S1).

Moderate interstitial pneumonia in K18-hACE2 mice following SARS-CoV-2 infection. To evaluate the effects of SARS-CoV-2 infection in the lower respiratory tract of K18-hACE2 mice, we performed similar analysis to that described above. In the lower respiratory tract, histologic alterations in the pulmonary parenchyma mainly involved the alveoli, interstitium and vasculature. Pathologic alterations in the lungs were overall characterized by variable degree of interstitial pneumonia and variable abundance of SARS-CoV-2 antigen and RNA, which were strictly dependent on the experimental timepoint.

At 2 dpi, mild perivascular and peribronchiolar inflammation, consisting primarily of lymphocytes and lesser numbers of histiocytes, and occasional perivascular edema were evident (Figure 3). Pulmonary vessels were frequently reactive and lined by a plump endothelium with large numbers of marginating mononuclear leukocytes and few neutrophils (Figure 3). Multifocal to coalescing areas of the pulmonary parenchyma, mostly associated with a bronchopulmonary segment, were composed of alveolar septa mildly expanded by lymphocytes, histiocytes and fewer neutrophils along with scattered air spaces containing low numbers of neutrophils and mild numbers of histiocytes and lymphocytes (Figure 3). SARS-CoV-2 antigen and RNA were multifocally detected within the pulmonary parenchyma, and localized in alveolar type (AT) 1 and fewer AT2 pneumocytes predominantly within and adjacent to areas of interstitial pneumonia as

demonstrated by singleplex and multiplex IHC, and RNAscope® ISH (Figure 3 and Figure S2).

At 4 dpi, peak in viral antigen and RNA abundance was reached (correlating with the highest viral RNA load as determined by RT-qPCR) along with a higher number of infiltrating lymphocytes (Figure 3 and Figure S2). SARS-CoV-2 cellular tropism did not differ from that described at 2 dpi.

At 7 dpi, there was an increase in the severity of the interstitial pneumonia, which affected up to ~30% of the parenchyma (Figure 3). Multifocal bronchopulmonary segments were composed of alveolar septa expanded by numerous mononuclear cells and fewer neutrophils that extend into the alveolar spaces, occasional septal necrotic debris, and mild proliferation of AT2 cells (Figure 3). In some animals, the affected alveoli were multifocally denuded to completely disrupted by necrosis, and filled with necrotic cell debris and alveolar edema. As for earlier timepoints, mild perivascular and peribronchiolar cuffing of lymphocytes and histiocytes was a common feature. While bronchioles were mostly unaffected, sporadically they were partially lined by an attenuated epithelium and contain rare, individualized mononuclear cells within their lumina. SARS-CoV-2 antigen and RNA were still abundant (Figure 3, Table 1, Figure S2, and Table S1), albeit to a lower extent than at 4 dpi suggesting progressive resolution of viral infection by the host consistent with the RT-qPCR data (Figure 1E). Interestingly, viral antigen was mostly distributed in AT1 and AT2 cells within histologically normal areas of lung adjacent to areas of intense inflammation, while areas of subacute interstitial pneumonia and mild AT2 hyperplasia were characterized by scant to absent SARS-CoV-2 S immunoreactivity (Figure 3, Table 1 and Table S1).

Finally, multifocal areas of similar interstitial pneumonia with sporadic aggregates of interstitial lymphocytes and more prominent AT2 hyperplasia were identified in the two male survivors at 14 dpi (Figure 3). No SARS-CoV-2 antigen or RNA was detected at this time point (Figure 3 and Figure S2).

Of note, no evidence of SARS-CoV-2 infection in bronchiolar epithelium and pulmonary vasculature was seen at any time during the course of the study (Figure 3, Table 1, Figure S2, and Table S1). Similarly, hyaline membranes, vascular thrombosis, and syncytial cells were not observed at any time point across all animals; which strikingly contrasts with the human patient (Martines et al., 2020) and non-human primate studies (Aid et al., 2020; Blair et al., 2020). Hemorrhage and pulmonary edema were only rarely observed and of minimal-to-moderate severity. In one animal (7 dpi), there was localized flooding of bronchioles by degenerate neutrophils and cellular debris mixed with birefringent foreign material consistent with aspiration pneumonia, a reported rare complication in K18 hACE2 mice infected with SARS-CoV-1 that is ultimately attributed to pharyngeal and laryngeal dysfunction secondary to central nervous system (CNS) disease (McCray et al., 2007).

Altogether, our data shows evidence of a significant but moderate interstitial pneumonia in infected K18-hACE2 mice. The histopathological features and the moderate extent of the pneumonia observed in the lung of K18-hACE2 mice therefore contrast with those observed in severe cases of COVID-19 in humans, and suggest that the lethality observed in this model might be independent of lung inflammatory mechanisms.

Effective control of SARS-CoV-2 infection in the lower respiratory tract is associated with T-cell and macrophage infiltration. Subsequently, we aimed to further investigate SARS-CoV-2 tropism in the lower respiratory tract of K18-hACE2 mice, as well as the dynamics of the host response in this tissue upon infection. We first performed multiplex IHC to probe the localization of SARS-CoV-2 antigen in AT1 pneumocytes (cell maker: receptor for advanced glycation end-products [RAGE]), AT2 pneumocytes (cell marker: surfactant protein C [SPC]), and endothelial cells (cell marker: CD31). We found that SARS-CoV-2 showed preferential tropism for RAGE+ AT1 pneumocytes, as well as scattered SPC+ AT2 pneumocytes, but not for CD31+ endothelial cells (Figure 4A).

Next, we optimized and applied a 5-plex IHC to characterize the inflammatory response in the lungs of K18-hACE2 mice infected with SARS-CoV-2. At 2 dpi, the affected areas of the pulmonary parenchyma were characterized by abundant viral antigen accompanied by an early host response predominantly mediated by Iba-1+ macrophages and low numbers of CD3+CD8- T lymphocytes (presumably CD4+ T lymphocytes, Figure 4C). At 7 dpi, the parenchyma was infiltrated by CD3+CD8+ and CD3+CD8- T lymphocytes and abundant Iba-1+ macrophages with a reduction in the number of SARS-CoV-2-infected cells, the latter mostly restricted to areas of the parenchyma with less intense inflammatory response (Figure 4D). At 14 dpi, the inflammatory response was characterized by multifocal interstitial aggregates of CD19+ B lymphocytes, abundant Iba-1+ macrophages, moderate numbers of CD3+CD8- T lymphocytes, (scattered throughout the interstitium as well as associated with CD19+ B lymphocyte aggregates) and a reduction in the number of infiltrating CD3+CD8+ T

lymphocytes with undetectable SARS-CoV-2 antigen (Figure 4E). Altogether, our data showed that control of SARS-CoV-2 in the lung of K18-hACE2 mice is associated with moderate interstitial pneumonia characterized by a strong local lymphocytic and histiocytic host response. Effective immune control and moderate inflammation once again suggest that lethality observed in K18-hACE2 mice is attributable to lung-independent disease.

Severe SARS-CoV-2 neuroinvasion and neurological damage in K18-hACE2 mice.

Pursuing our hypothesis that the lethality of the K18-hACE2 mice is associated with brain neuroinvasion, we analyzed sagittal sections of the brain including representation of the cribriform plate and olfactory bulb at different timepoints post-infection (2, 4, 6-7 and 14 dpi) for histologic changes and viral antigen distribution (Figures 5 and 6). Histologic alterations in the brain were first observed as early as 6 dpi but mostly at 7 dpi, and consisted of mild, multifocal neuronal spongiosis primarily throughout the cerebral cortical layers of the somatomotor, somatosensory and visual areas (Figure 5). Additionally, multifocal blood vessels were delimited by delicate cuffs of few lymphocytes with mild numbers of reactive glial cells in the adjacent neuroparenchyma. At 7 dpi, histologic alterations worsened in severity and became more widespread with involvement of the olfactory bulb, cerebral cortex (most predominantly somatosensory and somatomotor areas), hippocampus (mainly CA1 region), brainstem (thalamus), midbrain and the dentate nucleus ventral to the cerebellum (Figure 5). At the level of the olfactory bulb, the glomerular, external plexiform, and mitral cell layers were characterized by moderate to marked neuropil vacuolization (spongiosis) with occasional vacuoles containing intralesional cell debris. Elsewhere, the grey and white

matter within affected areas of the neuroparenchyma were extensively and predominantly characterized by marked spongiosis with frequent clear vacuoles containing intralesional cell debris, and multifocal shrunken, angular, hypereosinophilic and pyknotic neuronal bodies with loss of Nissl substance/chromatolysis (neuronal degeneration and necrosis, Figure 5) and occasionally delimited by multiple glial cells (satellitosis). There were multifocal, delicate perivascular cuffs composed of lymphocytes and the adjacent neuroparenchyma had an increase in the number of reactive glial cells (gliosis). Notably, the cerebellum (cortical layers and associated white matter of the cerebellar folia) was spared of histologic changes.

Neuronal changes correlated with abundant neuronal immunoreactivity for SARS-CoV-2 S antigen and viral RNA, with exclusive localization within the perikaryon and neuronal processes (Figure 6). SARS-CoV-2 antigen and RNA had a widespread distribution throughout the brain in roughly 85% (11/13) of infected K18-hACE2 mice at 7 dpi, including neuronal bodies within the cerebral cortex, CA1, CA2 and CA3 regions of the hippocampus, anterior olfactory nucleus, caudoputamen, nucleus accumbens, thalamic nuclei including hypothalamus, midbrain, pons and medulla oblongata nuclei (Figure 6). Few vestibulocochlear nerve fascicles showed immunoreactivity for viral antigen; while no viral S antigen or RNA was detected in areas spared of histological changes including the cerebellar cortex and white matter, optic nerve and retina, and the spiral ganglion of the inner ear (albeit the eye and inner ear were not present in the majority of sections examined). SARS-CoV-2 S antigen and RNA preceded histological findings with rare viral antigen and RNA detected as early as 4 dpi in mitral and inner nuclear

neurons of the olfactory bulb, as well as small clusters of neurons within the anterior olfactory nucleus and orbital area of the cerebral cortex (Figure 6).

Multiplex IHC for co-detection of SARS-CoV-2 antigen, Iba-1+ and GFAP+ glial cells was performed at 7 dpi, timepoint at which widespread viral antigen and RNA along with histological lesions were observed. Multiple IHC revealed that the gliosis in the brain of infected mice was attributed to abundant GFAP+ astrocytes as well as Iba-1+ microglial cells, which did not colocalize with SARS-CoV-2 S protein expression (Figure 7). Iba-1+ microglial cells with broad cytoplasmic ramifications were seen to be tightly associated with SARS-CoV-2+ neuronal bodies, suggestive of an active host response against infection (Figure 7).

We evaluated the extent of the CNS involvement in infected K18-hACE2 mice at 7 dpi by additionally examining the cervicothoracic and lumbosacral segments of the spinal cord. In 9/11 infected K18-hACE2 mice that showed widespread viral antigen in the brain, the spinal cord also had mild-to-moderate viral antigen that predominated within the cervicothoracic segments (Figure S3, Table 1 and Table S1). Neuronal changes were similar to those noted in affected areas of the brain; however, gliosis and perivascular cuffing were sparse.

Finally, Luxol Fast Blue was utilized to assess myelin loss (demyelination) following SARS-CoV-2 invasion in the brain and spinal cord at 7 dpi. No evidence of demyelination was noted.

Taken together, our data show that SARS-CoV-2 infection of K18-hACE2 results in severe neuronal invasion of the CNS, likely via retrograde transport through the

olfactory bulb originating from axonal processes traversing the ONE. Viral neuroinvasion resulted in extensive cytopathic effect in neurons, comprising not only the brain but also the spinal cord.

ACE2 expression and distribution does not fully reflect SARS-CoV-2 tissue tropism in K18-hACE2 mice. To further explore the mechanism driving lethal SARS-CoV-2 infection in K18-hACE2 mice, we first investigated the tissue and cellular distribution of the ACE2 receptor in both C57BL/6J and K18-hACE2 mice by IHC using a cross-reactive anti-ACE2 antibody (cross-reactive to hACE2 and mACE2) (Table S2). In the lower respiratory tract (lungs), ACE2 was ubiquitously expressed along the apical membrane of bronchiolar epithelium and, less commonly, in rare and scattered AT2 pneumocytes (Figure 8). No ACE2 expression was found in AT1 pneumocytes. Strikingly, no differences in the distribution and abundance of ACE2 expression were identified between uninfected C57BL/6J, sham-inoculated K18-hACE2, and terminal (7 dpi) K18-hACE2 mice inoculated with SARS-CoV-2 (Figure 8).

We therefore aimed at analyzing expression and distribution of *hACE2* mRNA using RNAscope® ISH. Although no expression of *hACE2* mRNA was detected in the lungs of non-transgenic C57BL/6J mice (Figure 9), expression of *hACE2* mRNA was detectable but low in the lungs of K18-hACE2 mice, and mostly involved bronchiolar epithelial cells with sporadic expression within few pneumocytes (Figure 9). In summary, these findings indicate that *hACE2* expression in the lungs of K18-hACE2 is low, and that expression of *hACE2* is not the sole host factor determinant of susceptibility to SARS-CoV-2. This is clearly exemplified by the following: 1) certain cell types that, while expressing

394 *hACE2,* were non-permissive to SARS-CoV-2 infection throughout the experiment (i.e.
395 bronchiolar epithelial cells); and 2) the near diffuse infection of AT1 cells by 4 dpi
396 despite sparse to absent expression of *hACE2* in these cells. These observations
397 support evidence for an ACE2-independent viral entry mechanism playing a major role
398 in the pulmonary dissemination of K18-hACE2 mice.

399 In contrast to the lung, increased ACE2 expression was clearly evident in the nasal
400 cavity of K18-hACE2 mice compared to C57BL/6J mice. We assessed ACE2
401 expression on the rostral nasal epithelium, respiratory epithelium at the level of the
402 intermediate turbinates (Figure 8) as well as in the ONE and olfactory bulb (Figure 8).
403 Unlike C57BL/6J mice, in which ACE2 was undetectable within the nasal cavity, ACE2
404 was diffusely expressed within the apical membrane of transitional and respiratory
405 epithelium, and segmentally within the apical surface of the ONE in both sham-
406 inoculated and SARS-CoV-2-infected K18-hACE mice (Figure 8). While minimal to rare
407 expression of *hACE2* mRNA was identified in the neurons of the mitral layer of the
408 olfactory bulb, olfactory neuroepithelium and respiratory epithelium of rostral turbinates,
409 estimation of its abundance and distribution could not be fully assessed since the
410 decalcification procedure had a significant impact in the quality of cellular mRNA as
411 demonstrated by the low detection of the housekeeping mRNA, *Ppib* (data not shown).

412 In the brain of both C57BL/6J and K18-hACE2 mice, ACE2 immunoreactivity was
413 observed in the vascular endothelium lining blood vessels (Figure 8), as well as
414 ependymal and choroid plexus epithelium. In contrast, distribution of *hACE2* mRNA
415 expression involved clusters of neurons within the cerebral cortex, hippocampus,
416 midbrain, brainstem and Purkinje cells from the cerebellum, with no expression noted in

non-transgenic C57BL/6J mice (Figure 10 and Figure S4). There was no expression of *hACE2* mRNA in vascular endothelial cells. Taken together, our data show a discrepancy between ACE2 protein and RNA expression and distribution within the CNS. This is partly attributable to the fact that the ACE2 antibody we utilized cross reacts with both hACE2 and mACE2, while the *ACE2* probe employed was human specific. The absence of *hACE2* hybridization with simultaneous ACE2 immunoreactivity in the capillary endothelium supports the notion that ACE2 expression in these cells is of murine origin. The absence of ACE2 immunoreactivity in neurons is suggestive of a potential restriction in the translation (or post-translation) of the ACE2 receptor in these cells. This, in addition to the fact that Purkinje cells of the cerebellum are non-permissive to SARS-CoV-2 infection in spite of the expression of *hACE2* mRNA, also suggests that ACE2 is likely not the sole host factor associated with neuroinvasion and that other ACE2-independent entry mechanisms contribute to neuroinvasion and spread by SARS-CoV-2 in this murine model.

Absence of infection and histologic lesions in extrapulmonary and extraneural tissues despite ACE2 expression. Other tissues examined included heart, kidney, stomach, duodenum, jejunum, ileum, cecum, and colon. All of these were histologically within normal limits (data not shown). No SARS-CoV-2 S antigen was detected in any of these tissues at any time point (data not shown). ACE2 distribution was evaluated in sections of the heart, stomach, small intestine and colon. While ACE2 expression was limited to the capillary vascular endothelium in the heart and stomach, intense expression was noted in the non-glandular mucosa of the stomach and apical surface of

enterocytes lining the small intestinal mucosa. Colonic enterocytes rarely expressed ACE2 (Figure S5).

DISCUSSION

The K18-hACE2 transgenic mouse model has become a widespread laboratory animal model suitable for studying SARS-CoV-2 pathogenesis as well as medical countermeasures against COVID-19 (Johansen et al., 2020). The suitability of this model relies on the common host entry receptor shared between SARS-CoV-1 and SARS-CoV-2 (Hoffmann et al., 2020; Li et al., 2003), and transgenic mice expressing hACE2 under the K18 promoter develop lethal clinical disease associated with pulmonary pathology and neuroinvasion, with high viral titers (Golden et al., 2020; McCray et al., 2007; Moreau et al., 2020; Oladunni et al., 2020; Rathnasinghe et al., 2020; Winkler et al., 2020; Yinda et al., 2020; Zheng et al., 2020). In contrast, other murine models of SARS-CoV-2 (e.g. adenovirus-transduced hACE2 mice and transgenic mice expressing hACE2 under the HFH4 promoter) develop only mild disease with limited and short-lived viral replication and pulmonary pathology, and low to no lethality (Jiang et al., 2020; Rathnasinghe et al., 2020). While the K18-hACE2 murine model has been critical in shedding light on mechanisms of lung injury and dysfunction, it fails to faithfully recapitulate several key histologic features of severe and lethal cases of COVID-19 in humans, such as diffuse alveolar damage (DAD) with hyaline membrane formation and multi-organ failure associated with hypercoagulability and widespread microthrombi formation (Maiese et al., 2020; Martines et al., 2020).

In order to better understand the pathogenesis of SARS-CoV-2, well-characterized animal models are critically needed (Munoz-Fontela et al., 2020). Even though the K18-hACE2 murine model is currently under extensive use, several aspects associated with the temporospatial dynamics of SARS-CoV-2 infection remain poorly characterized, including the expression and cellular distribution of hACE2. We attempted to further characterize pathological aspects related to viral pathogenesis in this unique murine model, and hypothesized that the temporospatial distribution of SARS-CoV-2 and pathological outcomes following infection in the K18-hACE2 murine model is partially but not solely associated with hACE2 and that increased lethality in this model is related to neuroinvasion. The study presented herein provides additional novel information regarding the temporal and spatial aspects of SARS-CoV-2 infection in the K18-hACE2 mouse model with emphasis on pathological outcomes as well as a thorough and methodical characterization of ACE2 expression in this transgenic mouse model, which contributes to our understanding of this critical model used for preclinical evaluation of vaccines and antiviral therapeutics. The results presented herein not only demonstrate that lethality of this murine model is associated with neuroinvasion and subsequent neuronal cytopathic effect, but that SARS-CoV-2 tropism is not solely restricted to ACE2-expressing cells in K18-hACE2 mice. Thus, the neuropathogenic potential of SARS-CoV-2 is dependent on other host factors.

In this study, we have utilized a large cohort of K18-hACE2 mice (n=50) in order to sequentially evaluate SARS-CoV-2 tropism and pathological alterations, spatial and temporal analysis of host factors including inflammatory response and ACE2/*hACE2* expression, and survival curve analysis for a period of 14 dpi. Similarly to previous

studies, which only observed the outcome of SARS-CoV-2 for up to 7 dpi (Golden et al., 2020; Moreau et al., 2020; Oladunni et al., 2020; Rathnasinghe et al., 2020; Winkler et al., 2020), infected K18-hACE2 mice initially developed significant clinical disease with marked weight loss and increased respiratory effort associated with the development of interstitial pneumonia and high viral load as determined via IHC, ISH and RT-qPCR; an unquestionable feature of this model. Survival curve analysis clearly demonstrated that lethality in infected mice only occurs after 6 dpi and in the vast majority of mice (96.3%), coincided with the initiation of neurologic signs and/or symptoms, neuronal cytopathic effect, and abundance of viral S antigen and RNA in the CNS. These observations are a clear indication of the rapid and fatal neuroinvasive nature of this model. Our study also demonstrates that SARS-CoV-2 has a tropism for motor neurons within the spinal cord (predominantly within the cervicothoracic segments), which was only observed in mice with concurrent brain involvement suggesting a descending infection. This finding helps rationalize the neurologic signs observed with this model including decreased mobility/responsiveness and decreased urine voiding that was evident at necropsy, reflective of severe urinary bladder dilation and accumulation of concentrated urine. Given the spinal cord involvement, the latter is likely attributed to altered spinal reflexes and/or decreased intervention of the detrusor muscle, which is required for normal micturation. An additional striking clinical feature in infected K18-hACE2 mice at 7 dpi was hypothermia (mean body temperature of 30.6 °C), which is likely a consequence of hypothalamic and motor neuron dysfunction associated with SARS-CoV-2 neurotropism and could serve as a clinical indicator of CNS involvement. Our results unequivocally demonstrate that neuroinvasion represents the driving component of fatality in this

508 animal model compared to others such as Syrian hamsters, which display more severe
509 pulmonary disease and infection of the ONE, but no evidence of neuroinvasion (Bryche
510 et al., 2020). Furthermore, these animals invariably recover within 14 days following
511 intranasal infection with SARS-CoV-2 (Bryche et al., 2020; Imai et al., 2020; Osterrieder
512 et al., 2020; Rosenke et al., 2020; Sia et al., 2020). Very few infected K18-hACE2 mice
513 (2/30) from our cohort survived until the end of the study (14 dpi) and, while ameliorated
514 pulmonary lesions were noticed in these, they did not exhibit involvement of the CNS
515 further supporting the observation that mice suffering from SARS-CoV-2 neuroinvasion
516 invariably succumb at earlier time points post-infection. Both of these survivor mice
517 developed pulmonary interstitial aggregates of B lymphocytes that were distinct from
518 earlier time points, which could be suggestive of the development of protective adaptive
519 immunity. The normal histologic appearance of the CNS in surviving mice and lack of
520 any residual neurologic signs supports the notion that animals can fully recover from
521 infection, albeit we acknowledge that limited neuroinvasion in these animals could not
522 be disproven. Furthermore, we acknowledge that extensive neurobehavior testing,
523 which is beyond the expertise of the authors, would be required to rule out any long-
524 term sequelae in the rare instance of survivors. Overall, these findings are of
525 importance to researchers with a particular interest in studying SARS-CoV-2-associated
526 neuropathogenesis, as premature euthanasia due to other clinical features (i.e., weight
527 loss, ruffled fur, and/or respiratory distress) have the potential to precede CNS disease
528 and such terminal endpoints, if elected, may preclude evaluation of the effects of SARS-
529 CoV-2 in the CNS. Instead decreased responsiveness/mobility and tremors are
530 interpreted to reflect better clinical findings supportive of neuroinvasive disease.

To date, the precise mechanism(s) enabling neuroinvasion in the K18-hACE2 model is poorly understood (Bryche et al., 2020; DosSantos et al., 2020; Ellul et al., 2020; Liu et al., 2020; Solomon et al., 2020). Here, we determined that K18-hACE2 transgenic mice show a significant upregulation in the expression of ACE2 in the nasal cavity (particularly in the neuroepithelium) compared to wild-type C57BL/6J mice, in which ACE2 expression is undetectable by IHC. This difference between K18-hACE2 and C57BL/6J mice is clearly attributed to the expression of the *hACE2* transgene, and is a key feature to the neuropathogenesis of this model. Interestingly, temporal analysis of SARS-CoV-2 S antigen and RNA in the ONE of transgenic mice preceded and/or occurred simultaneously with infection of neurons within the glomerular and mitral layers of the olfactory bulb, indicative of possible viral retrograde transport through axonal processes traversing the cribriform plate and allowing viral spread within cortical neurons and beyond. Expression of *hACE2* within neurons in the CNS is overall low and does not correlate with our immunohistochemical findings, where ACE2 protein was restricted to capillary endothelium, ependymal and choroid epithelium with sparing of neurons and their processes. These findings suggest the ACE2 expression in these anatomical compartments could be attributed to *mACE2* or indicative of a post-transcriptional event that could be limiting neuronal expression of *hACE2*. These along with the fact that *hACE2* mRNA is not abundantly and equally expressed among different neuronal populations and that Purkinje cells in the cerebellum express *hACE2* mRNA, but are not permissive to SARS-CoV-2 infection, suggest that entry of SARS-CoV-2 into neurons is likely mediated by other host receptors independent of ACE2.

553 Infection of brain organoids has been shown to be inhibited by the use of anti-ACE2
554 antibodies (Song et al., 2020). However, brain organoids do not recapitulate the
555 complexity of the entire CNS, and retrograde transport of viral particles into the CNS
556 can hardly be modeled *in vitro*. Altogether, this suggests that while ACE2 is assuredly
557 an important mediator of CNS neuroinvasion, *in vitro* platforms to study mechanisms of
558 SARS-CoV-2 neuroinvasion are limiting, and require the use of more complex
559 experimental systems. Recently, neuropilin-1, a transmembrane glycoprotein serving as
560 cell surface receptor for semaphorins and other ligands, was shown to serve as an
561 alternative receptor for SARS-CoV-2 mediating entry into the neuroepithelium and
562 neurons (Cantuti-Castelvetri et al., 2020). Even though we analyzed the expression of
563 neuropilin-1 in this study (data not shown), we observed ubiquitous expression in the
564 nasal passages, brain, kidneys, liver and lungs, precluding any definitive conclusions in
565 support or against these claims (Cantuti-Castelvetri et al., 2020).
566 Anosmia and ageusia (loss of smell and taste, respectively) represent the earliest and
567 most common but transient neurologic symptoms in people with COVID-19, being
568 reported in ≥ 50% of cases (Eliezer et al., 2020; Ellul et al., 2020; Walker et al., 2020).
569 Hyposmia or anosmia has also been clearly characterized in K18-hACE2 mice,
570 occurring between 2-3 dpi, which was characterized through a series of unique
571 behavioral tests requiring a normal sense of smell (Zheng et al., 2020). Other neurologic
572 manifestations of COVID-19 are associated with acute cerebrovascular disease, with
573 cohort studies reporting strokes in 2–6% of hospitalized patients (Ellul et al., 2020;
574 Wang et al., 2020b). Long-term neurologic sequelae associated with COVID-19 or its
575 effect on neurodegenerative diseases remain unclear (Wang et al., 2020b). Very little is

known about the pathogenesis of these neurologic manifestations and whether they are directly or indirectly associated with SARS-CoV-2. ACE2 expression has been described in humans both in health and with chronic rhinosinusitis, with expression noted in sustentacular cells of the ONE, but not within immature and mature olfactory neurons (Chen et al., 2020). This observation led the authors to suggest that anosmia in COVID-19 is likely attributable to an indirect effect of SARS-CoV-2 infection. However, recent studies evaluated brain and nasal autopsies from patients who died of COVID-19, in which SARS-CoV-2 antigen and RNA was detected in cells of neural origin within the ONE and cortical neurons occasionally associated with locally ischemic regions (Meinhardt et al., 2020; Song et al., 2020). These studies provide conclusive evidence that the K18-hACE2 mice serves as a model with translational significance, even though ischemic lesions have not been reported including those in our study, further justifying its use to dissect the intricate mechanisms involved in SARS-CoV-2-mediated CNS invasion. Even though SARS-CoV-2 infects sustentacular cells within the neuroepithelium of Syrian hamsters (Bryche et al., 2020), the K18-hACE2 and a CRISPR/Cas9 hACE2 knock-in mouse model (Sun et al., 2020) are the only models that develop neuroinvasion with wild-type virus and, thus, will be particularly useful for studying SARS-CoV-2 neuropathogenesis, particularly the mechanisms of viral trafficking of into the CNS through the neuroepithelium.

Another important observation of the K18-hACE2 model is that SARS-CoV-2 tropism extensively involves infection of ACE2 and *hACE2* negative cells, including certain population of neurons and the vast majority of AT1 pneumocytes. Similarly, sole expression of *hACE2* in some cell types (i.e., bronchiolar epithelial cells) clearly does

not render these cells susceptible to SARS-CoV-2 even following intranasal exposure, and underscore that other undetermined host factors are most likely required to allow viral entry. Therefore, this model is extremely relevant for investigating the role of ACE2-independent entry.

In conclusion, this study provides a comprehensive spatiotemporal analysis of SARS-CoV-2 infection in the K18-hACE2 transgenic murine model along with an analysis of the contribution of ACE2 in the permissiveness of the model. Our work provides evidence that SARS-CoV-2 exhibits a marked neurotropism, and that this process likely occurs through mechanisms that are in part hACE2-independent. Lethal CNS invasion, combined with the absence of several of the pulmonary hallmarks associated with severe human COVID-19, therefore calls for attentive caution when utilizing the K18-hACE2 mouse model to investigate certain aspects of SARS-CoV-2 pathogenesis. The protective ability of anti-viral therapies and T-cell based vaccines against lethal challenge in this model might indeed be then underestimated due to the increased susceptibility to CNS invasion. Regardless, the K18-hACE2 mouse model represents a promising model for understanding the mechanisms governing SARS-CoV-2 neuroinvasion, ACE2-independent virus entry, and evaluating potent and fast-acting prophylactic countermeasures.

MATERIALS AND METHODS

Biosafety. All aspects of this study were approved by the Institutional Biosafety Committee and the office of Environmental Health and Safety at Boston University prior

621 to study initiation. Work with SARS-CoV-2 was performed in a biosafety level-3
622 laboratory by personnel equipped with powered air-purifying respirators.

623 **Cells and viruses.** African green monkey kidney Vero E6 cells (ATCC® CRL-1586™,
624 American Type Culture Collection, Manassas, VA) were maintained in Dulbecco's
625 minimum essential medium (DMEM; Gibco, Carlsbad, CA [#11995-065]) containing
626 10% fetal bovine serum (FBS, ThermoFisher Scientific, Waltham, MA), 1X non-essential
627 amino acids (ThermoFisher Scientific), penicillin and streptomycin (100 U/ml and 100
628 µg/ml), and 0.25 µg/ml of amphotericin B (Gibco®, Carlsbad, CA), and incubated at 37
629 °C and 5% CO_2 in a humidified incubator.

630 **SARS-CoV-2 isolate stock preparation and titration.** All replication-competent
631 SARS-CoV-2 experiments were performed in a biosafety level 3 laboratory (BSL-3) at
632 the Boston University' National Emerging Infectious Diseases Laboratories. 2019-
633 nCoV/USA-WA1/2020 isolate (NCBI accession number: MN985325) of SARS-CoV-2
634 was obtained from the Centers for Disease Control and Prevention (Atlanta, GA) and
635 BEI Resources (Manassas, VA). To generate the passage 1 (P1) virus stock, Vero E6
636 cells, pre-seeded the day before at a density of 10 million cells, were infected in T175
637 flasks with the master stock, diluted in 10 ml final volume of Opti-MEM (ThermoFisher
638 Scientific). Following virus adsorption to the cells at 37 ºC for 1 h, 15 ml DMEM
639 containing 10% FBS and 1X penicillin/streptomycin was added to the flask. The next
640 day, media was removed, the cell monolayer was rinsed with 1X phosphate buffered
641 saline (PBS) pH 7.5 (ThermoFisher Scientific) and 25 ml of fresh DMEM containing 2%
642 FBS was added. Two days later, when the cytopathic effect of the virus was clearly
643 visible, culture medium was collected, filtered through a 0.2 µm filter, and stored at -80

ºC. Our P2 working stock of the virus was prepared by infecting Vero E6 cells with the P1 stock, at a multiplicity of infection (MOI) of 0.1. Cell culture media was harvested at 2 and 3 dpi, and after the last harvest, ultracentrifuged (Beckman Coulter Optima L-100k; SW32 Ti rotor) for 2 h at 25,000 rpm (80,000 *X* g) over a 20% sucrose cushion (Sigma-Aldrich, St. Louis, MO). Following centrifugation, the media and sucrose were discarded and pellets were left to dry for 5 minutes at room temperature. Pellets were then resuspended overnight at 4 ºC in 500 µl of 1X PBS. The next day, concentrated virions were aliquoted at stored at -80 ºC.

The titer of our viral stock was determined by plaque assay. Vero E6 cells were seeded into a 12-well plate at a density of 2.5 x 10^5 cells per well and infected the next day with serial 10-fold dilutions of the virus stock for 1 h at 37 ºC. Following virus adsorption, 1 ml of overlay media, consisting of 2X DMEM supplemented with 4% FBS and mixed at a 1:1 ratio with 1.2% Avicel (DuPont; RC-581), was added in each well. Three days later, the overlay medium was removed, the cell monolayer was washed with 1X PBS and fixed for 30 minutes at room temperature with 4% paraformaldehyde (Sigma-Aldrich). Fixed cells were then washed with 1X PBS and stained for 1h at room temperature with 0.1% crystal violet (Sigma-Aldrich) prepared in 10% ethanol/water. After rinsing with tap water, the number of plaques were counted and the virus titer was calculated. The titer of our P2 virus stock was 4 x 10^8 plaque forming units (PFU)/ml.

Mice. Mice were maintained in a facility accredited by the Association for the Assessment and Accreditation of Laboratory Animal Care (AAALAC). All protocols were approved by the Boston University Institutional Animal Care and Use Committee (PROTO202000020). Heterozygous K18-hACE2 C57BL/6J mice of both sexes (strain:

667 2B6.Cg-Tg(K18-ACE2)2Prlmn/J) were obtained from the Jackson Laboratory (Jax, Bar
668 Harbor, ME). Animals were group-housed by sex in Tecniplast green line individually
669 ventilated cages (Tecniplast, Buguggiate, Italy). Mice were maintained on a 12:12 light
670 cycle at 30-70% humidity and provided ad-libitum water and standard chow diets
671 (LabDiet, St. Louis, MO).

672 **Intranasal inoculation with SARS-CoV-2.** At 4 months of age, K18-hACE2 mice of
673 both sexes were intranasally inoculated with 1 x 10^6 PFU of SARS-CoV-2 in 50 µl of
674 sterile 1X PBS (n=47 [n=25 male and n=12 female), or sham inoculated with 50 µl of
675 sterile 1X PBS (n=3; female). Inoculations were performed under 1-3% isoflurane
676 anesthesia. Animals were either enrolled in a 14-day survival curve study (n=33).
677 Animals were only euthanized early if they reached euthanasia criteria, or if the
678 experiment included predetermined euthanasia timepoints for tissue sampling (2, 4, or 7
679 dpi; n=15).

680 **Clinical monitoring.** Animals included in the 14-day survival curve study were
681 intraperitoneally implanted with an RFID temperature-monitoring microchip (Unified
682 Information Devices, Lake Villa, IL, USA) 48-72 hours prior to inoculation. An IACUC-
683 approved clinical scoring system was utilized to monitor disease progression and
684 establish humane endpoints (Table 2). Categories evaluated included body weight,
685 general appearance, responsiveness, respiration, and neurological signs for a
686 maximum score of 5. Animals were considered moribund and humanely euthanized in
687 the event of the following: a score of 4 or greater for 2 consecutive observation periods,
688 weight loss greater than or equal to 20%, severe respiratory distress, or lack of

responsiveness. Clinical signs and body temperature were recorded once per day for the duration of the study.

Tissue processing and viral RNA isolation. Tissues were collected from mice and stored in 600 µl of RNA*later* (Sigma-Aldrich; # R0901500ML) and stored at -80 °C. For processing, 20 – 30 mg of tissue were placed into a 2 ml tube with 600 µl of RLT buffer with 1% β-mercaptoethanol and a 5 mm stainless steel bead (Qiagen, Valencia, CA; #69989). Tissues were then dissociated using a Qiagen TissueLyser II (Qiagen) with the following cycle parameters: 20 cycles/s for 2 min, 1 min wait, 20 cycles/s for 2 min. Samples were centrifuged at 17,000 *X* g (13,000 rpm) for 10 minutes and supernatant was transferred to a new 1.5 ml tube. Viral RNA isolation was performed using a Qiagen RNeasy Plus Mini Kit (Qiagen; #74134), according to the manufacturer's instructions, with an additional on-column DNase treatment (Qiagen; #79256). RNA was finally eluted in 30 µl of RNase/DNase-free water and stored at -80 °C until used.

RNA isolation from serum. Total viral RNA was isolated from serum using a Zymo Research Corporation Quick-RNA™ Viral Kit (Zymo Research, Tustin, CA; #R1040) according to the manufacturer's instructions. RNA was eluted in 15 µl of RNase/DNase-free water and stored at -80 °C until used.

SARS-CoV-2 E-specific reverse transcription quantitative polymerase chain reaction (RT-qPCR). Viral RNA was quantitated using single-step RT-quantitative real-time PCR (Quanta qScript One-Step RT-qPCR Kit, QuantaBio, Beverly, MA; VWR; #76047-082) with primers and TaqMan® probes targeting the SARS-CoV-2 E gene as previously described (Corman et al., 2020). Briefly, a 20 µl reaction mixture containing 10 µl of Quanta qScript™ XLT One-Step RT-qPCR ToughMix, 0.5 µM Primer

712 E_Sarbeco_F1 (ACAGGTACGTTAATAGTTAATAGCGT), 0.5 µM Primer
713 E_Sarbeco_R2 (ATATTGCAGCAGTACGCACACA), 0.25 µM Probe E_Sarbeco_P1
714 (FAM-ACACTAGCCATCCTTACTGCGCTTCG-BHQ1), and 2 µl of template RNA was
715 prepared. RT-qPCR was performed using an Applied Biosystems QuantStudio 3
716 (ThermoFisher Scientific) and the following cycling conditions: reverse transcription for
717 10 minutes at 55 °C, an activation step at 94 °C for 3 min followed by 45 cycles of
718 denaturation at 94 °C for 15 seconds and combined annealing/extension at 58 °C for 30
719 seconds. Ct values were determined using QuantStudio™ Design and Analysis software
720 V1.5.1 (ThermoFisher Scientific). For absolute quantitation of viral RNA, a 389 bp
721 fragment from the SARS-CoV-2 E gene was cloned onto pIDTBlue plasmid under an
722 SP6 promoter using NEB PCR cloning kit (New England Biosciences, Ipswich, MA).
723 The cloned fragment was then *in vitro* transcribed (mMessage mMachine SP6
724 transcription kit; ThermoFisher) to generate an RT-qPCR standard.

725 **Serum infectivity assay.** Vero E6 cells were plated in a 24-well plate at a density of
726 50,000 cells per well. To assess for infectious particles, 20 µl of serum was added onto
727 cells with 250 µl of DMEM supplemented with 2% FBS and 1% penicillin and
728 streptomycin and incubated for 6 hours at 37 °C. After incubation, serum was removed,
729 cells were washed twice with 1 ml of 1X PBS, and 1 ml of DMEM supplemented with
730 2% FBS 1% penicillin and streptomycin was added to each well. Media was collected
731 24- and 96-hours post infection for RT-qPCR analysis.

732 **Histology.** Animals were anesthetized with 1-3% isoflurane and euthanized with an
733 intraperitoneal overdose of ketamine and xylazine before harvest and fixation of tissues.
734 Lungs were insufflated with ~1.5mL of 1% low melting point agarose (Sigma-Aldrich)

diluted in 1X PBS using a 24-gauge catheter placed into the trachea. The skull cap was removed and the animal decapitated and immersed in fixative. Additional tissues harvested included the heart, kidneys, and representative sections of the gastrointestinal tract, which included the duodenum, jejunum, ileum, cecum, and colon. Tissues were inactivated in 10% neutral buffered formalin at a 20:1 fixative to tissue ratio for a minimum of 72 hours before removal from BSL-3 in accordance with an approved institutional standard operating procedure. Following fixation, the whole head was decalcified in Immunocal™ Decalcifier (StatLab, McKinney, TX) for 7 days before performing a mid-sagittal section dividing the two hemispheres into even sections. Tissues were subsequently processed and embedded in paraffin following standard histological procedures. Five-micron sections were obtained and stained with hematoxylin and eosin or Luxol Fast Blue (myelin stain).

Immunohistochemistry and RNAscope® *in situ* hybridization. Immunohistochemistry (IHC) was performed using a Ventana BenchMark Discovery Ultra autostainer (Roche Diagnostics, Indianapolis, IN) using tyramide signaling amplification (TSA) technology. Specific IHC assay details including antibodies, antigen retrieval, sequence of multiplex assays, and incubation periods are found in Table S2. SARS-CoV-2 S was semiquantitatively scored as follows: 0, no viral antigen observed; 1, up to 5% positive cells per 400X field examined; 2, 5-25% positive cells per 400X field examined; and 3, up to 50% positive cells per 400X field examined.

For SARS-CoV-2 RNAscope® ISH, an anti-sense probe targeting the spike (S; nucleotide sequence: 21,563-25,384) of SARS-CoV-2, USA-WA1/2020 isolate (GenBank accession number MN985325.1) was used as previously described

(Carossino et al., 2020; Gaudreault et al., 2020). The RNAscope® ISH assay was performed using the RNAscope 2.5 LSx Reagent Kit (Advanced Cell Diagnostics, Newark, CA) on the automated BOND RXm platform (Leica Biosystems, Buffalo Grove, IL) as described previously (Meekins et al., 2020). Briefly, four-micron sections of formalin-fixed paraffin-embedded tissue were subjected to automated baking and deparaffinization followed by heat-induced epitope retrieval (HIER) using a ready-to-use EDTA-based solution (pH 9.0; Leica Biosystems) at 100 °C for 15 min. Subsequently, tissue sections were treated with a ready-to-use protease (RNAscope® 2.5 LSx Protease) for 15 min at 40 °C followed by a ready-to-use hydrogen peroxide solution for 10 min at room temperature. Slides were then incubated with the ready-to-use probe mixture for 2 h at 40 °C, and the signal amplified using a specific set of amplifiers (AMP1 through AMP6 as recommended by the manufacturer). The signal was detected using a Fast-Red solution for 10 minutes at room temperature. Slides were counterstained with a ready-to-use hematoxylin for 5 min, followed by five washes with 1X BOND Wash Solution (Leica Biosystems) for bluing. Slides were finally rinsed in deionized water, dried in a 60 °C oven for 30 min, and mounted with Ecomount® (Biocare, Concord, CA, USA). A SARS-CoV-2-infected Vero E6 cell pellet was used as a positive assay control. For all assays, an uninfected mouse was used as a negative control.

For *hACE2* mRNA RNAscope® ISH, an anti-sense probe targeting *hACE2* (GenBank accession number NM_021804.3; Cat. No. 848038) with no cross-reactivity to murine *Ace2* was used in a similar manner as described above with the exception that AMP5 and AMP6 were incubated for 45 min and 30 min, respectively. Murine *peptidylprolyl*

isomerase B (Ppib) mRNA was used as a housekeeping gene to determine RNA quality and a Vero E6 cell pellet was used as a positive assay control.

Multispectral microscopy. Fluorescently labeled slides were imaged using a Mantra 2.0™ Quantitative Pathology Workstation (Akoya Biosciences, Marlborough, MA). To maximize signal-to-noise ratios, images were spectrally unmixed using a synthetic library specific for the Opal fluorophores used for each assay and for 4′,6-diamidino-2-phenylindole (DAPI). Furthermore, an unstained section was used to create an autofluorescence signature that was subsequently removed from whole-slide images using InForm software version 2.4.8 (Akoya Biosciences).

Statistical analysis. Descriptive statistics and graphics as well as Kaplan-Meier (survival) curves and statistical tests were performed using GraphPad Prism statistical analysis software (GraphPad, San Diego, CA). Clinical parameters were analyzed using a Student *t*-test. Significance levels were set at p-value<0.05 in all cases.

FUNDING

We thank the Evans Center for Interdisciplinary Biomedical Research at Boston University School of Medicine for their support of the Affinity Research Collaborative on 'Respiratory Viruses: A Focus on COVID-19'. This work utilized a Ventana Discovery Ultra autostainer that was purchased with funding from a National Institutes of Health SIG grant (S10-OD026983). This work was also supported by a Boston University Start-up fund, and a Peter Paul Career Development Professorship (to F.D.). This study was also partially supported by start-up funds provided by the School of Veterinary Medicine,

Louisiana State University to Dr. Udeni Balasuriya (PG002165) and by pilot funding to Dr. Markus Bosmann from the National Institutes of Health grant 1UL1TR001430.

CONFLICT OF INTEREST STATEMENT

The authors declare no conflicts of interest.

AUTHOR CONTRIBUTIONS: F. Douam, N. Crossland, M. Carossino, U. Balasuriya and M. Bosmann designed the study; F. Douam, N Crossland, M. Saeed, M. Carossino, P. Montanaro, A. O'Connell, D. Kenney, H. Gertje, K Grosz, and S Kurnick performed the experiments; F. Douam, N. Crossland, M. Carossino, P. Montanaro, A. O'Connell, and D. Kenney performed data analysis; and M. Carossino, N. Crossland, and F. Douam wrote the manuscript.

ACKNOWLEDGEMENTS

Drs. Crossland and Carossino would like to thank our pathology mentors Drs. Fabio Del Piero and Ingeborg M. Langohr for helping instill our passion for pathology and for introducing us to each other. We are hopeful these efforts will represent the early days of a fruitful and long-lasting collaboration. We acknowledge the Histology and Immunohistochemistry sections at the Louisiana Animal Disease Diagnostic Laboratory for their technical assistance. The following reagent was deposited by the Centers for Disease Control and Prevention and obtained through BEI Resources, NIAID, NIH: SARS-Related Coronavirus 2, Isolate USA-WA1/2020, NR-52281.

REFERENCES

827 Aid, M., K. Busman-Sahay, S.J. Vidal, Z. Maliga, S. Bondoc, C. Starke, M. Terry, C.A. Jacobson, L. Wrijil, S.
828 Ducat, O.R. Brook, A.D. Miller, M. Porto, K.L. Pellegrini, M. Pino, T.N. Hoang, A. Chandrashekar,
829 S. Patel, K. Stephenson, S.E. Bosinger, H. Andersen, M.G. Lewis, J.L. Hecht, P.K. Sorger, A.J.
830 Martinot, J.D. Estes, and D.H. Barouch. 2020. Vascular Disease and Thrombosis in SARS-CoV-2-
831 Infected Rhesus Macaques. *Cell* 183:1354-1366 e1313.
832 Andersen, K.G., A. Rambaut, W.I. Lipkin, E.C. Holmes, and R.F. Garry. 2020. The proximal origin of SARS-
833 CoV-2. *Nat Med* 26:450-452.
834 Blair, R.V., M. Vaccari, L.A. Doyle-Meyers, C.J. Roy, K. Russell-Lodrigue, M. Fahlberg, C.J. Monjure, B.
835 Beddingfield, K.S. Plante, J.A. Plante, S.C. Weaver, X. Qin, C.C. Midkiff, G. Lehmicke, N. Golden, B.
836 Threeton, T. Penney, C. Allers, M.B. Barnes, M. Pattison, P.K. Datta, N.J. Maness, A. Birnbaum, T.
837 Fischer, R.P. Bohm, and J. Rappaport. 2020. Acute Respiratory Distress in Aged, SARS-CoV-2-
838 Infected African Green Monkeys but Not Rhesus Macaques. *Am J Pathol*
839 Bryche, B., A. St Albin, S. Murri, S. Lacote, C. Pulido, M. Ar Gouilh, S. Lesellier, A. Servat, M. Wasniewski,
840 E. Picard-Meyer, E. Monchatre-Leroy, R. Volmer, O. Rampin, R. Le Goffic, P. Marianneau, and N.
841 Meunier. 2020. Massive transient damage of the olfactory epithelium associated with infection
842 of sustentacular cells by SARS-CoV-2 in golden Syrian hamsters. *Brain Behav Immun* 89:579-586.
843 Cantuti-Castelvetri, L., R. Ojha, L.D. Pedro, M. Djannatian, J. Franz, S. Kuivanen, F. van der Meer, K. Kallio,
844 T. Kaya, M. Anastasina, T. Smura, L. Levanov, L. Szirovicza, A. Tobi, H. Kallio-Kokko, P. Osterlund,
845 M. Joensuu, F.A. Meunier, S.J. Butcher, M.S. Winkler, B. Mollenhauer, A. Helenius, O. Gokce, T.
846 Teesalu, J. Hepojoki, O. Vapalahti, C. Stadelmann, G. Balistreri, and M. Simons. 2020. Neuropilin-
847 1 facilitates SARS-CoV-2 cell entry and infectivity. *Science* 370:856-860.
848 Carossino, M., H.S. Ip, J.A. Richt, K. Shultz, K. Harper, A.T. Loynachan, F. Del Piero, and U.B.R. Balasuriya.
849 2020. Detection of SARS-CoV-2 by RNAscope((R)) in situ hybridization and
850 immunohistochemistry techniques. *Arch Virol* 165:2373-2377.
851 Chen, M., W. Shen, N.R. Rowan, H. Kulaga, A. Hillel, M. Ramanathan, Jr., and A.P. Lane. 2020. Elevated
852 ACE-2 expression in the olfactory neuroepithelium: implications for anosmia and upper
853 respiratory SARS-CoV-2 entry and replication. *Eur Respir J* 56:
854 Conceicao, C., N. Thakur, S. Human, J.T. Kelly, L. Logan, D. Bialy, S. Bhat, P. Stevenson-Leggett, A.K.
855 Zagrajek, P. Hollinghurst, M. Varga, C. Tsirigoti, M. Tully, C. Chiu, K. Moffat, A.P. Silesian, J.A.
856 Hammond, H.J. Maier, E. Bickerton, H. Shelton, I. Dietrich, S.C. Graham, and D. Bailey. 2020. The
857 SARS-CoV-2 Spike protein has a broad tropism for mammalian ACE2 proteins. *PLoS Biol*
858 18:e3001016.
859 Corman, V.M., O. Landt, M. Kaiser, R. Molenkamp, A. Meijer, D.K. Chu, T. Bleicker, S. Brunink, J.
860 Schneider, M.L. Schmidt, D.G. Mulders, B.L. Haagmans, B. van der Veer, S. van den Brink, L.
861 Wijsman, G. Goderski, J.L. Romette, J. Ellis, M. Zambon, M. Peiris, H. Goossens, C. Reusken, M.P.
862 Koopmans, and C. Drosten. 2020. Detection of 2019 novel coronavirus (2019-nCoV) by real-time
863 RT-PCR. *Euro Surveill* 25:
864 Coronaviridae Study Group of the International Committee on Taxonomy of, V. 2020. The species Severe
865 acute respiratory syndrome-related coronavirus: classifying 2019-nCoV and naming it SARS-CoV-
866 2. *Nat Microbiol* 5:536-544.
867 Damas, J., G.M. Hughes, K.C. Keough, C.A. Painter, N.S. Persky, M. Corbo, M. Hiller, K.P. Koepfli, A.R.
868 Pfenning, H. Zhao, D.P. Genereux, R. Swofford, K.S. Pollard, O.A. Ryder, M.T. Nweeia, K.
869 Lindblad-Toh, E.C. Teeling, E.K. Karlsson, and H.A. Lewin. 2020. Broad host range of SARS-CoV-2
870 predicted by comparative and structural analysis of ACE2 in vertebrates. *Proc Natl Acad Sci U S A*
871 117:22311-22322.
872 Dinnon, K.H., 3rd, S.R. Leist, A. Schafer, C.E. Edwards, D.R. Martinez, S.A. Montgomery, A. West, B.L.
873 Yount, Jr., Y.J. Hou, L.E. Adams, K.L. Gully, A.J. Brown, E. Huang, M.D. Bryant, I.C. Choong, J.S.
874 Glenn, L.E. Gralinski, T.P. Sheahan, and R.S. Baric. 2020. A mouse-adapted model of SARS-CoV-2

to test COVID-19 countermeasures. *Nature* In press (https://doi.org/10.1038/s41586-020-2708-8):

DosSantos, M.F., S. Devalle, V. Aran, D. Capra, N.R. Roque, J.d.M. Coelho-Aguiar, T.C.L.d.S.e. Spohr, J.G. Subilhaga, C.M. Pereira, I. D'Andrea Meira, P. Niemeyer Soares Filho, and V. Moura-Neto. 2020. Neuromechanisms of SARS-CoV-2: A Review. *Frontiers in Neuroanatomy* 14:

Eliezer, M., A.L. Hamel, E. Houdart, P. Herman, J. Housset, C. Jourdaine, C. Eloit, B. Verillaud, and C. Hautefort. 2020. Loss of smell in patients with COVID-19: MRI data reveal a transient edema of the olfactory clefts. *Neurology* 95:e3145-e3152.

Ellul, M.A., L. Benjamin, B. Singh, S. Lant, B.D. Michael, A. Easton, R. Kneen, S. Defres, J. Sejvar, and T. Solomon. 2020. Neurological associations of COVID-19. *Lancet Neurol* 19:767-783.

Gaudreault, N., J. Trujillo, M. Carossino, D. Meekins, D. Madden, V. Balaraman, J. Henningson, I. Morozov, D. Bold, T. Kwong, G. Roman-Sosa, B. Artiaga, S. Indran, K. Cool, A. Garcia-Sastre, W. Ma, W. Wilson, U. Balasuriya, and J. Richt. 2020. SARS-CoV-2 infection, disease and transmission in domestic cats. *Emerg Microbes Inf* In press (https://doi.org/10.1080/22221751.2020.1833687):

Golden, J.W., C.R. Cline, X. Zeng, A.R. Garrison, B.D. Carey, E.M. Mucker, L.E. White, J.D. Shamblin, R.L. Brocato, J. Liu, A.M. Babka, H.B. Rauch, J.M. Smith, B.S. Hollidge, C. Fitzpatrick, C.V. Badger, and J.W. Hooper. 2020. Human angiotensin-converting enzyme 2 transgenic mice infected with SARS-CoV-2 develop severe and fatal respiratory disease. *JCI Insight* 5:

Goyal, P., J.J. Choi, L.C. Pinheiro, E.J. Schenck, R. Chen, A. Jabri, M.J. Satlin, T.R. Campion, Jr., M. Nahid, J.B. Ringel, K.L. Hoffman, M.N. Alshak, H.A. Li, G.T. Wehmeyer, M. Rajan, E. Reshetnyak, N. Hupert, E.M. Horn, F.J. Martinez, R.M. Gulick, and M.M. Safford. 2020. Clinical Characteristics of Covid-19 in New York City. *N Engl J Med* 382:2372-2374.

Hoffmann, M., H. Kleine-Weber, S. Schroeder, N. Kruger, T. Herrler, S. Erichsen, T.S. Schiergens, G. Herrler, N.H. Wu, A. Nitsche, M.A. Muller, C. Drosten, and S. Pohlmann. 2020. SARS-CoV-2 Cell Entry Depends on ACE2 and TMPRSS2 and Is Blocked by a Clinically Proven Protease Inhibitor. *Cell* 181:271-280 e278.

Imai, M., K. Iwatsuki-Horimoto, M. Hatta, S. Loeber, P.J. Halfmann, N. Nakajima, T. Watanabe, M. Ujie, K. Takahashi, M. Ito, S. Yamada, S. Fan, S. Chiba, M. Kuroda, L. Guan, K. Takada, T. Armbrust, A. Balogh, Y. Furusawa, M. Okuda, H. Ueki, A. Yasuhara, Y. Sakai-Tagawa, T.J.S. Lopes, M. Kiso, S. Yamayoshi, N. Kinoshita, N. Ohmagari, S.I. Hattori, M. Takeda, H. Mitsuya, F. Krammer, T. Suzuki, and Y. Kawaoka. 2020. Syrian hamsters as a small animal model for SARS-CoV-2 infection and countermeasure development. *Proc Natl Acad Sci U S A* 117:16587-16595.

Jiang, R.D., M.Q. Liu, Y. Chen, C. Shan, Y.W. Zhou, X.R. Shen, Q. Li, L. Zhang, Y. Zhu, H.R. Si, Q. Wang, J. Min, X. Wang, W. Zhang, B. Li, H.J. Zhang, R.S. Baric, P. Zhou, X.L. Yang, and Z.L. Shi. 2020. Pathogenesis of SARS-CoV-2 in Transgenic Mice Expressing Human Angiotensin-Converting Enzyme 2. *Cell* 182:50-58 e58.

Johansen, M.D., A. Irving, X. Montagutelli, M.D. Tate, I. Rudloff, M.F. Nold, N.G. Hansbro, R.Y. Kim, C. Donovan, G. Liu, A. Faiz, K.R. Short, J.G. Lyons, G.W. McCaughan, M.D. Gorrell, A. Cole, C. Moreno, D. Couteur, D. Hesselson, J. Triccas, G.G. Neely, J.R. Gamble, S.J. Simpson, B.M. Saunders, B.G. Oliver, W.J. Britton, P.A. Wark, C.A. Nold-Petry, and P.M. Hansbro. 2020. Animal and translational models of SARS-CoV-2 infection and COVID-19. *Mucosal Immunol* 13:877-891.

Johns Hopkins University & Medicine. 2020. Coronavirus Resource Center. In.

Lee, M.H., D.P. Perl, G. Nair, W. Li, D. Maric, H. Murray, S.J. Dodd, A.P. Koretsky, J.A. Watts, V. Cheung, E. Masliah, I. Horkayne-Szakaly, R. Jones, M.N. Stram, J. Moncur, M. Hefti, R.D. Folkerth, and A. Nath. 2020. Microvascular Injury in the Brains of Patients with Covid-19. *N Engl J Med*

Li, W., M.J. Moore, N. Vasilieva, J. Sui, S.K. Wong, M.A. Berne, M. Somasundaran, J.L. Sullivan, K. Luzuriaga, T.C. Greenough, H. Choe, and M. Farzan. 2003. Angiotensin-converting enzyme 2 is a functional receptor for the SARS coronavirus. *Nature* 426:450-454.

Liu, J.M., B.H. Tan, S. Wu, Y. Gui, J.L. Suo, and Y.C. Li. 2020. Evidence of central nervous system infection and neuroinvasive routes, as well as neurological involvement, in the lethality of SARS-CoV-2 infection. *J Med Virol*

Maiese, A., A.C. Manetti, R. La Russa, M. Di Paolo, E. Turillazzi, P. Frati, and V. Fineschi. 2020. Autopsy findings in COVID-19-related deaths: a literature review. *Forensic Sci Med Pathol*

Martines, R.B., J.M. Ritter, E. Matkovic, J. Gary, B.C. Bollweg, H. Bullock, C.S. Goldsmith, L. Silva-Flannery, J.N. Seixas, S. Reagan-Steiner, T. Uyeki, A. Denison, J. Bhatnagar, W.J. Shieh, S.R. Zaki, and C.-P.W. Group. 2020. Pathology and Pathogenesis of SARS-CoV-2 Associated with Fatal Coronavirus Disease, United States. *Emerg Infect Dis* 26:2005-2015.

McCray, P.B., Jr., L. Pewe, C. Wohlford-Lenane, M. Hickey, L. Manzel, L. Shi, J. Netland, H.P. Jia, C. Halabi, C.D. Sigmund, D.K. Meyerholz, P. Kirby, D.C. Look, and S. Perlman. 2007. Lethal infection of K18-hACE2 mice infected with severe acute respiratory syndrome coronavirus. *J Virol* 81:813-821.

McNamara, T., J.A. Richt, and L. Glickman. 2020. A Critical Needs Assessment for Research in Companion Animals and Livestock Following the Pandemic of COVID-19 in Humans. *Vector Borne Zoonotic Dis*

Meekins, D.A., I. Morozov, J.D. Trujillo, N.N. Gaudreault, D. Bold, M. Carossino, B.L. Artiaga, S.V. Indran, T. Kwon, V. Balaraman, D.W. Madden, H. Feldmann, J. Henningson, W. Ma, U.B.R. Balasuriya, and J.A. Richt. 2020. Susceptibility of swine cells and domestic pigs to SARS-CoV-2. *Emerg Microbes Inf* In press (https://doi.org/10.1080/22221751.2020.1831405):

Meinhardt, J., J. Radke, C. Dittmayer, J. Franz, C. Thomas, R. Mothes, M. Laue, J. Schneider, S. Brunink, S. Greuel, M. Lehmann, O. Hassan, T. Aschman, E. Schumann, R.L. Chua, C. Conrad, R. Eils, W. Stenzel, M. Windgassen, L. Rossler, H.H. Goebel, H.R. Gelderblom, H. Martin, A. Nitsche, W.J. Schulz-Schaeffer, S. Hakroush, M.S. Winkler, B. Tampe, F. Scheibe, P. Kortvelyessy, D. Reinhold, B. Siegmund, A.A. Kuhl, S. Elezkurtaj, D. Horst, L. Oesterhelweg, M. Tsokos, B. Ingold-Heppner, C. Stadelmann, C. Drosten, V.M. Corman, H. Radbruch, and F.L. Heppner. 2020. Olfactory transmucosal SARS-CoV-2 invasion as a port of central nervous system entry in individuals with COVID-19. *Nat Neurosci*

Moreau, G.B., S.L. Burgess, J.M. Sturek, A.N. Donlan, W.A. Petri, and B.J. Mann. 2020. Evaluation of K18-hACE2 Mice as a Model of SARS-CoV-2 Infection. *Am J Trop Med Hyg* 103:1215-1219.

Munoz-Fontela, C., W.E. Dowling, S.G.P. Funnell, P.S. Gsell, A.X. Riveros-Balta, R.A. Albrecht, H. Andersen, R.S. Baric, M.W. Carroll, M. Cavaleri, C. Qin, I. Crozier, K. Dallmeier, L. de Waal, E. de Wit, L. Delang, E. Dohm, W.P. Duprex, D. Falzarano, C.L. Finch, M.B. Frieman, B.S. Graham, L.E. Gralinski, K. Guilfoyle, B.L. Haagmans, G.A. Hamilton, A.L. Hartman, S. Herfst, S.J.F. Kaptein, W.B. Klimstra, I. Knezevic, P.R. Krause, J.H. Kuhn, R. Le Grand, M.G. Lewis, W.C. Liu, P. Maisonnasse, A.K. McElroy, V. Munster, N. Oreshkova, A.L. Rasmussen, J. Rocha-Pereira, B. Rockx, E. Rodriguez, T.F. Rogers, F.J. Salguero, M. Schotsaert, K.J. Stittelaar, H.J. Thibaut, C.T. Tseng, J. Vergara-Alert, M. Beer, T. Brasel, J.F.W. Chan, A. Garcia-Sastre, J. Neyts, S. Perlman, D.S. Reed, J.A. Richt, C.J. Roy, J. Segales, S.S. Vasan, A.M. Henao-Restrepo, and D.H. Barouch. 2020. Animal models for COVID-19. *Nature* 586:509-515.

Oladunni, F.S., J.-G. Park, P.P. Tamayo, O. Gonzalez, A. Akhter, A. Allué-Guardia, A. Olmo-Fontánez, S. Gautam, A. Garcia-Vilanova, C. Ye, K. Chiem, C. Headley, V. Dwivedi, L.M. Parodi, K.J. Alfson, H.M. Staples, A. Schami, J.I. Garcia, A. Whigham, R.N. Platt, M. Gazi, J. Martinez, C. Chuba, S. Earley, O.H. Rodriguez, S.D. Mdaki, K.N. Kavelish, R. Escalona, C.R.A. Hallam, C. Christie, J.L. Patterson, T.J.C. Anderson, R. Carrion, E.J. Dick, S. Hall-Ursone, L.S. Schlesinger, D. Kaushal, L.D. Giavedoni, X. Alvarez, J. Turner, L. Martinez-Sobrido, and J.B. Torrelles. 2020. Lethality of SARS-

969 CoV-2 infection in K18 human angiotensin converting enzyme 2 transgenic mice. *bioRxiv*
970 preprint (https://doi.org/10.1101/2020.07.18.210179):
971 Osterrieder, N., L.D. Bertzbach, K. Dietert, A. Abdelgawad, D. Vladimirova, D. Kunec, D. Hoffmann, M.
972 Beer, A.D. Gruber, and J. Trimpert. 2020. Age-Dependent Progression of SARS-CoV-2 Infection in
973 Syrian Hamsters. *Viruses* 12:
974 Rathnasinghe, R., S. Strohmeier, F. Amanat, V.L. Gillespie, F. Krammer, A. Garcia-Sastre, L. Coughlan, M.
975 Schotsaert, and M.B. Uccellini. 2020. Comparison of transgenic and adenovirus hACE2 mouse
976 models for SARS-CoV-2 infection. *Emerg Microbes Infect* 9:2433-2445.
977 Rockx, B., T. Kuiken, S. Herfst, T. Bestebroer, M.M. Lamers, B.B. Oude Munnink, D. de Meulder, G. van
978 Amerongen, J. van den Brand, N.M.A. Okba, D. Schipper, P. van Run, L. Leijten, R. Sikkema, E.
979 Verschoor, B. Verstrepen, W. Bogers, J. Langermans, C. Drosten, M. Fentener van Vlissingen, R.
980 Fouchier, R. de Swart, M. Koopmans, and B.L. Haagmans. 2020. Comparative pathogenesis of
981 COVID-19, MERS, and SARS in a nonhuman primate model. *Science* 368:1012-1015.
982 Rosenke, K., K. Meade-White, M. Letko, C. Clancy, F. Hansen, Y. Liu, A. Okumura, T.L. Tang-Huau, R. Li, G.
983 Saturday, F. Feldmann, D. Scott, Z. Wang, V. Munster, M.A. Jarvis, and H. Feldmann. 2020.
984 Defining the Syrian hamster as a highly susceptible preclinical model for SARS-CoV-2 infection.
985 *bioRxiv*
986 Shi, J., Z. Wen, G. Zhong, H. Yang, C. Wang, B. Huang, R. Liu, X. He, L. Shuai, Z. Sun, Y. Zhao, P. Liu, L.
987 Liang, P. Cui, J. Wang, X. Zhang, Y. Guan, W. Tan, G. Wu, H. Chen, and Z. Bu. 2020. Susceptibility
988 of ferrets, cats, dogs, and other domesticated animals to SARS-coronavirus 2. *Science* 368:1016-
989 1020.
990 Shuai, L., G. Zhong, Q. Yuan, Z. Wen, C. Wang, X. He, R. Liu, J. Wang, Q. Zhao, Y. Liu, N. Huo, J. Deng, J.
991 Bai, H. Wu, Y. Guan, J. Shi, K. Tian, N. Xia, H. Chen, and Z. Bu. 2020. Replication, pathogenicity,
992 and transmission of SARS-CoV-2 in minks. *National Science Review*
993 Sia, S.F., L.M. Yan, A.W.H. Chin, K. Fung, K.T. Choy, A.Y.L. Wong, P. Kaewpreedee, R. Perera, L.L.M. Poon,
994 J.M. Nicholls, M. Peiris, and H.L. Yen. 2020. Pathogenesis and transmission of SARS-CoV-2 in
995 golden hamsters. *Nature* 583:834-838.
996 Simonnet, A., M. Chetboun, J. Poissy, V. Raverdy, J. Noulette, A. Duhamel, J. Labreuche, D. Mathieu, F.
997 Pattou, M. Jourdain, Licorn, C. the Lille, and g. Obesity study. 2020. High Prevalence of Obesity in
998 Severe Acute Respiratory Syndrome Coronavirus-2 (SARS-CoV-2) Requiring Invasive Mechanical
999 Ventilation. *Obesity (Silver Spring)* 28:1195-1199.
1000 Solomon, I.H., E. Normandin, S. Bhattacharyya, S.S. Mukerji, K. Keller, A.S. Ali, G. Adams, J.L. Hornick, R.F.
1001 Padera, and P. Sabeti. 2020. Neuropathological Features of Covid-19. *New England Journal of*
1002 *Medicine*
1003 Song, E., C. Zhang, B. Israelow, A. Lu-Culligan, A.V. Prado, S. Skriabine, P. Lu, O.E. Weizman, F. Liu, Y. Dai,
1004 K. Szigeti-Buck, Y. Yasumoto, G. Wang, C. Castaldi, J. Heltke, E. Ng, J. Wheeler, M.M. Alfajaro, E.
1005 Levavasseur, B. Fontes, N.G. Ravindra, D. Van Dijk, S. Mane, M. Gunel, A. Ring, S.A. Jaffar Kazmi,
1006 K. Zhang, C.B. Wilen, T.L. Horvath, I. Plu, S. Haik, J.L. Thomas, A. Louvi, S.F. Farhadian, A. Huttner,
1007 D. Seilhean, N. Renier, K. Bilguvar, and A. Iwasaki. 2020. Neuroinvasion of SARS-CoV-2 in human
1008 and mouse brain. *bioRxiv*
1009 Sun, S.H., Q. Chen, H.J. Gu, G. Yang, Y.X. Wang, X.Y. Huang, S.S. Liu, N.N. Zhang, X.F. Li, R. Xiong, Y. Guo,
1010 Y.Q. Deng, W.J. Huang, Q. Liu, Q.M. Liu, Y.L. Shen, Y. Zhou, X. Yang, T.Y. Zhao, C.F. Fan, Y.S. Zhou,
1011 C.F. Qin, and Y.C. Wang. 2020. A Mouse Model of SARS-CoV-2 Infection and Pathogenesis. *Cell*
1012 *Host Microbe* 28:124-133 e124.
1013 Tartof, S.Y., L. Qian, V. Hong, R. Wei, R.F. Nadjafi, H. Fischer, Z. Li, S.F. Shaw, S.L. Caparosa, C.L. Nau, T.
1014 Saxena, G.K. Rieg, B.K. Ackerson, A.L. Sharp, J. Skarbinski, T.K. Naik, and S.B. Murali. 2020.
1015 Obesity and Mortality Among Patients Diagnosed With COVID-19: Results From an Integrated
1016 Health Care Organization. *Ann Intern Med* In press (https://doi.org/10.7326/M20-3742):

1017 Team, C.C.-R. 2020. Preliminary Estimates of the Prevalence of Selected Underlying Health Conditions
1018 Among Patients with Coronavirus Disease 2019 - United States, February 12-March 28, 2020.
1019 *MMWR Morb Mortal Wkly Rep* 69:382-386.
1020 Tenforde, M.W., S.S. Kim, C.J. Lindsell, E. Billig Rose, N.I. Shapiro, D.C. Files, K.W. Gibbs, H.L. Erickson, J.S.
1021 Steingrub, H.A. Smithline, M.N. Gong, M.S. Aboodi, M.C. Exline, D.J. Henning, J.G. Wilson, A.
1022 Khan, N. Qadir, S.M. Brown, I.D. Peltan, T.W. Rice, D.N. Hager, A.A. Ginde, W.B. Stubblefield,
1023 M.M. Patel, W.H. Self, L.R. Feldstein, I.V.Y.N. Investigators, C.C.-R. Team, and I.V.Y.N.
1024 Investigators. 2020. Symptom Duration and Risk Factors for Delayed Return to Usual Health
1025 Among Outpatients with COVID-19 in a Multistate Health Care Systems Network - United States,
1026 March-June 2020. *MMWR Morb Mortal Wkly Rep* 69:993-998.
1027 Walker, A., G. Pottinger, A. Scott, and C. Hopkins. 2020. Anosmia and loss of smell in the era of covid-19.
1028 *BMJ* 370:m2808.
1029 Wang, C., P.W. Horby, F.G. Hayden, and G.F. Gao. 2020a. A novel coronavirus outbreak of global health
1030 concern. *Lancet* 395:470-473.
1031 Wang, F., R.M. Kream, and G.B. Stefano. 2020b. Long-Term Respiratory and Neurological Sequelae of
1032 COVID-19. *Med Sci Monit* 26:e928996.
1033 Winkler, E.S., A.L. Bailey, N.M. Kafai, S. Nair, B.T. McCune, J. Yu, J.M. Fox, R.E. Chen, J.T. Earnest, S.P.
1034 Keeler, J.H. Ritter, L.I. Kang, S. Dort, A. Robichaud, R. Head, M.J. Holtzman, and M.S. Diamond.
1035 2020. SARS-CoV-2 infection in the lungs of human ACE2 transgenic mice causes severe
1036 inflammation, immune cell infiltration, and compromised respiratory function. *Nature* In press
1037 (https://doi.org/10.1038/s41590-020-0778-2):
1038 Yinda, C.K., J.R. Port, T. Bushmaker, I.O. Owusu, V.A. Avanzato, R.J. Fischer, J.E. Schulz, M.G. Holbrook,
1039 M.J. Hebner, R. Rosenke, T. Thomas, A. Marzi, S.M. Best, E. de Wit, C. Shaia, N. van Doremalen,
1040 and V.J. Munster. 2020. K18-hACE2 mice develop respiratory disease resembling severe COVID-
1041 19. *bioRxiv* preprint (10.1101/2020.08.11.246314):
1042 Zheng, J., L.R. Wong, K. Li, A.K. Verma, M.E. Ortiz, C. Wohlford-Lenane, M.R. Leidinger, C.M. Knudson,
1043 D.K. Meyerholz, P.B. McCray, Jr., and S. Perlman. 2020. COVID-19 treatments and pathogenesis
1044 including anosmia in K18-hACE2 mice. *Nature*

1045

1046 ## FIGURE LEGENDS

1047 **Figure 1.** SARS-CoV-2 caused lethal disease in K18-hACE2 mice (n=33) inoculated
1048 intranasally with 1 x 10^6 plaque forming units (PFU). Body weight (A), clinical signs (B),
1049 temperature (C), and mortality (D) were monitored daily. Viral loads (genome copy
1050 numbers/mg or ml) were monitored in the brain, lungs (E) and serum (F) throughout the
1051 study. Mean genome copy numbers are depicted. The limit of detection (LOD) is shown
1052 with a dashed line.

Figure 2. Temporal analysis of SARS-CoV-2 infection in the nasal cavity of K18-hACE2 mice at 2 (A-D) and 4 (E-H) days following intranasal inoculation. Histological changes and viral antigen (brown) and RNA (red) distribution and abundance were assessed. At 2 dpi, suppurative rhinitis in the rostral and intermediate turbinates (A, arrow) correlated with abundant intraepithelial SARS-CoV-2 antigen (C) and RNA (C, inset). Abundant viral antigen and RNA was detected in the olfactory neuroepithelium (ONE, D and inset) in the absence of histologic lesions (B). At 4 dpi, only sporadically infected cells were noted in the epithelium lining the turbinates and ONE (G and H, arrow and insets) in the absence of histologic lesions (E and F). H&E and Fast Red (viral RNA), 200X total magnification. Bar = 100 µm.

Figure 3. Temporal analysis of SARS-CoV-2 infection in the lungs of K18-hACE2 mice at 2 (D-F), 4 (G-I), 7 (J-L) and 14 (M-O) days following intranasal inoculation. Histological changes and viral RNA (red) distribution and abundance were assessed. Mild to moderate interstitial pneumonia was evident starting at 2 days post-infection (dpi) with frequently reactive blood vessels (E, arrow) and a peak in viral RNA at 4 days post-infection (I). At 7 and 14 days post-infection, there was evidence of alveolar type 2 (AT2) cell hyperplasia (K and N, arrows), with viral RNA restricted to areas spared of inflammation (L). The pneumonia was significantly ameliorated by 14 dpi (M) with no viral RNA (O). H&E and Fast Red (viral RNA), 50X (A, D, G, J, and M; bar = 500 µm) and 200X (B, C, E, F, H, I, K, L, M and N; bar = 100 µm) total magnification.

Figure 4. SARS-CoV-2 tropism and temporal immunoprofiling of the pulmonary host inflammatory response following SARS-CoV-2 intranasal inoculation in K18-hACE2. (A) SARS-CoV-2 (yellow) showed tropism for $RAGE^{+}$ alveolar type 1 (AT1, magenta) and

scattered SPC^+ alveolar type 2 (AT2, red) pneumocytes (A1 and A2, arrowheads and arrows, respectively) but not for $CD31^+$ endothelial cells (green). SARS-CoV-2 (orange) was abundant and localized within AT1 and AT2 pneumocytes, with a progressive increase in the number of CD3+CD8- T cells (blue, presumed to be CD4+ T cells), Iba-1+ histiocytes (magenta), and CD8+ T cells (red) throughout the course of the experiment (2 days post-infection [dpi, C], 7 dpi [D] and 14 dpi [E]). SARS-CoV-2 S antigen was no longer detectable by 14 dpi, and numerous aggregates of CD19+ B cells (green) were noted (E). Multiplex fluorescent IHC, 200X total magnification. Bar = 50 µm

Figure 5. Temporal neuronal damage in K18-hACE2 mice following intranasal inoculation with SARS-CoV-2. No histologic changes were noted in the cerebrum or olfactory bulb until 6-7 days post-infection (dpi, A-D). SARS-CoV-2 antigen (brown) was evident as early as 4 dpi (F, arrow). At 6-7 dpi, mild (G, arrowheads) to marked (G, inset) spongiosis with neuronal degeneration and necrosis involving multiple areas within the cerebral cortex and elsewhere were noted. Similar changes were evident in the olfactory bulb, with occasional perivascular cuffs/gliosis (H, arrowhead) and abundant viral antigen (I, arrows). No histologic alterations or viral antigen was detected in survivor mice at 14 dpi (J-L). H&E and DAB (viral antigen), 100X (A, B, D, E, G, H, J, K; bar = 200 µm) and 200X (C, F, I, L; bar = 100 µm) total magnification.

Figure 6. Invasion of SARS-CoV-2 into the central nervous system. Sagittal sections of the head were analyzed for viral antigen and RNA distribution. SARS-CoV-2 infected neurons within the mitral layer of the olfactory bulb (1, arrow) as well as small clusters of neuronal bodies within the cerebral cortex (2, SARS-CoV-2 RNA in inset) as early as

4 days post-infection. At 7 days post-infection, SARS-CoV-2 antigen was widespread along the mitral layer of the olfactory bulb (1) and throughout the central nervous system (2, SARS-CoV-2 RNA in inset) with exception of the cerebellum. EPL, external plexiform layer; GCL, granular cell layer; GL, glomerular layer; ML, mitral layer. DAB (viral antigen) and Fast Red (viral RNA). 7.5X (bar = 2.5 mm) and 200X (bar = 100 µm) total magnification.

Figure 7. Analysis of SARS-CoV-2 tropism within the central nervous system at 7 days post-infection using multiplex immunohistochemistry. Abundant SARS-CoV-2 antigen (green) localized within cortical (A), hippocampal (B) and brainstem (C) neurons with abundant neighboring Iba-1+ microglia (orange) and clusters of GFAP+ astrocytes (gliosis, magenta). 40X total magnification. Bar = 50 µm.

Figure 8. Distribution of ACE2 in lungs, nasal cavity, brain and olfactory bulb of wild-type C57BL/6J and transgenic (mock and SARS-CoV-2-infected) K18-hACE2 mice was analyzed via immunohistochemistry using a cross-reactive anti-ACE2 antibody. In the lungs (A-C), ACE2 expression (brown) was mostly restricted to the apical membrane of bronchiolar epithelial cells with scattered positive pneumocytes (inset arrows). Nasal (rostral/intermediate turbinates [R/I]) and olfactory epithelium (ONE) were devoid of ACE2 in C57BL/6J mice (D) but expression was enhanced in K18-hACE2 mice with intense apical expression (E and F). ACE2 expression within the brain (G-I) and olfactory bulb (J-L) was restricted to capillary endothelium with no neuronal expression. DAB, 200X total magnification. Bar = 100 µm.

Figure 9. Expression and distribution of *hACE2* mRNA in the lungs of C57BL/6J and K18-hACE2 transgenic mice via RNAscope® ISH. While no expression of *hACE2* was

noted in the lungs of wild-type C57BL/6J mice (A), *hACE2* was expressed in the bronchiolar epithelium (arrowheads) and sporadic pneumocytes (arrows) in transgenic K18-hACE2 mice (B and C), which correlated with immunohistochemical findings. Fast Red, 400X total magnification. Bar = 50 µm.

Figure 10. Expression and distribution of *hACE2* mRNA in the brain of K18-hACE2 transgenic mice via RNAscope® ISH. *hACE2* was expressed in clusters of neurons within the cerebral cortex (A), hippocampus (B) as well as in other locations including Purkinje cells of the cerebellum. Fast Red, 400X total magnification. Bar = 50 µm.

SUPPLEMENTARY FIGURES

Figure S1. Histologic and viral antigen distribution in the nasal cavity of K18-hACE2 mice following SARS-CoV-2 infection. No histologic lesions or antigen were detected at 7 and 14 days post-infection (dpi). 200X total magnification. Bar = 100 µm.

Figure S2. Localization and abundance of SARS-CoV-2 RNA (red) and antigen (brown) in the lungs of infected K18-hACE2 mice as demonstrated by anti-Spike RNAscope® *in situ* hybridization and immunohistochemistry. 2 (A and B), 4 (C and D), 7 (E and F) and 14 (G and H) days post-infection (dpi). 50X (bar = 500 µm) and 100X (bar = 100 µm) total magnification.

Figure S3. Histological and immunohistochemical findings in the cervicothoracic spinal cord of SARS-CoV-2-infected K18-hACE2 mice at 7 days post-infection. Histologically (A), Multifocal neuronal bodies within the grey matter are shrunken, angular and hyperchromatic (neuronal degeneration and necrosis), and the neuroparenchyma has multiple clear spaces filled with small amounts of debris (spongiosis) with a slight

increase in the number of glial cells (gliosis). H&E, 100X total magnification. (B) Abundant SARS-CoV-2 spike protein localized within the perikaryon and processes of motor neurons within the spinal cord. DAB, 200X total magnification. Bar = 100 µm.

Figure S4. Expression of *hACE2* mRNA (red) in the brain of C57BL/6J and K18-hACE2 mice determined by RNAscope® ISH. While wild-type mice exhibit no expression (A), hACE2 is expressed in clusters of neurons at multiple locations in K18-hACE2 mice (B). Fast Red, 400X total magnification. Bar = 50 µm.

Figure S5. Expression of ACE2 (red) in the enterocytes lining the small intestine of C57BL/6J and K18-hACE2 mice. Immunohistochemistry was performed using a cross-reactive anti-ACE2 antibody. In the stomach, expression was intense in the non-glandular mucosa and capillaries of the glandular mucosa (A-C, arrows). In the colon, scattered enterocytes express ACE2 (G-I, arrows). Fast Red, 100X (A-C; bar = 200 µm) and 200X (D-I; bar = 100 µm) total magnification.

Table 1. SARS-CoV-2 viral antigen abundance in tissues derived from SARS-CoV-2-infected K18-hACE2 mice. Median scores are represented along with ranges between brackets when applicable.

DPI	AT1/AT2	Bronchioles	Rostral turbinates	Intermediate turbinates	ONE	Olf. bulb	Brain	Spinal cord (CT)	Spinal cord (LS)	GI*	Kidneys
Mock	0	0	0	0	0	0	0	0	0	0	0
2	2 (1-2)	0	1 (0-2)	2 (1-2)	1 (1-2)	0	0	0	0	0	0
4	2 (1-3)	0	0 (0-1)	0 (0-1)	1 (0-1)	0 (0-1)	0 (0-1)	0	0	0	0
6-8	2 (1-3)	0	0	0	1 (0-1)	1 (0-2)	3 (0-3)	1 (0-2)	0 (0-1)	0	0
14	0	0	0	0	0	0	0	0	0	0	0

0, no SARS-CoV-2 antigen observed; 1, 0 to 5% of cells within a high magnification (400X) field are positive for viral antigen; 2, 5 to 25% of cells within a high magnification (400X) field are positive for viral antigen; 3, >25 to <50% of cells within a high magnification (400X) field are positive for viral antigen. NA, not available. AT1, alveolar type 1 pneumocytes; AT2, alveolar type 2 pneumocytes; ONE, olfactory neuroepithelium; CT, cervicothoracic segment; LS, lumbosacral segment; GI, gastrointestinal tract.

*Sections examined included stomach, small intestine (duodenum, jejunum and ileum) and large intestine (cecum and colon).

1170 **Table 2.** Clinical scoring system used for clinical monitoring of SARS-CoV-2-infected K18-hACE2 mice.

Category	Score = Criteria
Body weight	1 = 10-19% loss
Respiration	1 = rapid, shallow, increased effort
Appearance	1 = ruffled fur, hunched posture
Responsiveness	1 = low to moderate unresponsiveness
Neurologic signs	1 = tremors

1171

1172

Figure 1

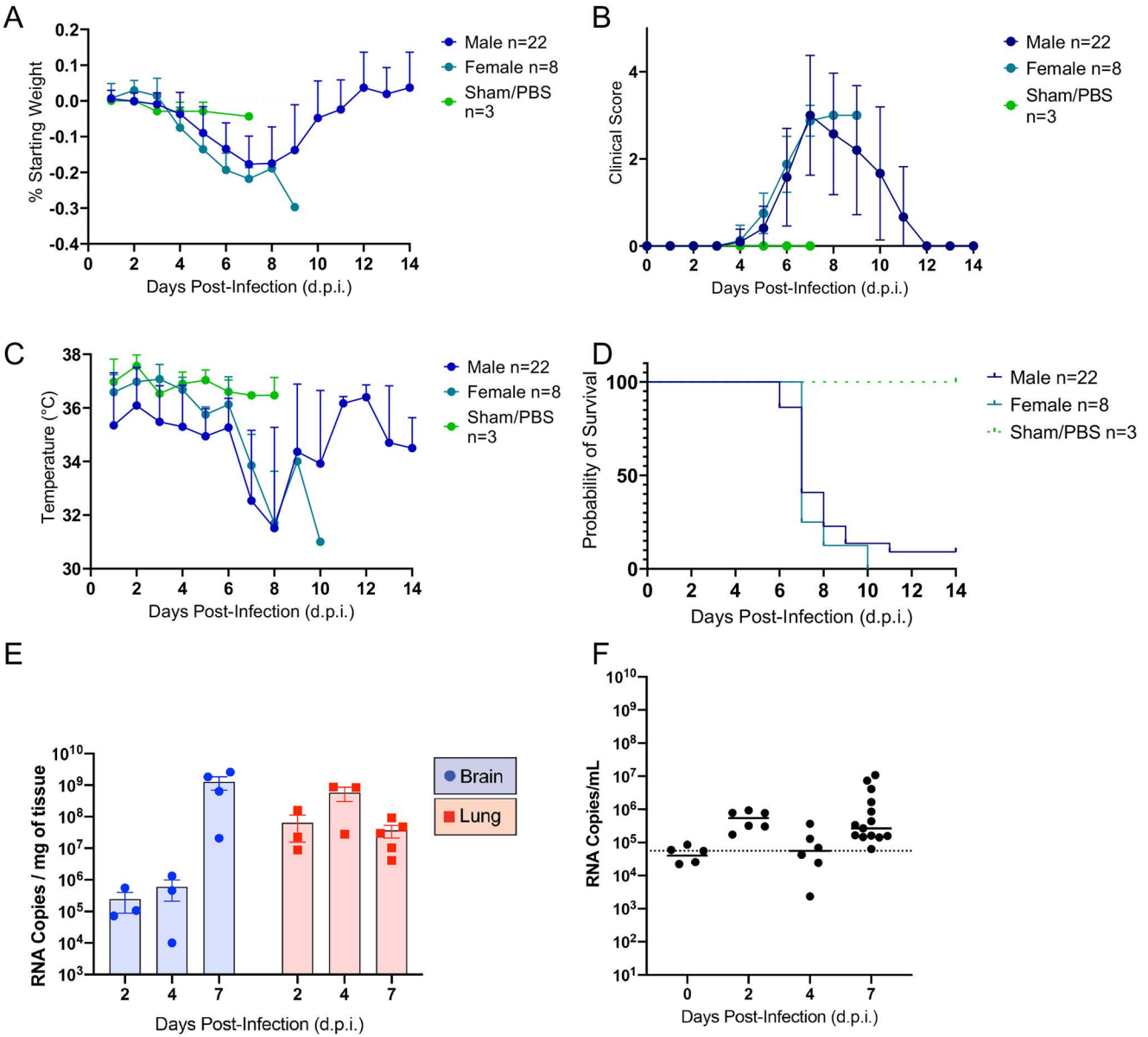
A
% Starting Weight
Days Post-Infection (d.p.i.)
Male n=22
Female n=8
Sham/PBS n=3
B
Clinical Score
Days Post-Infection (d.p.i.)
Male n=22
Female n=8
Sham/PBS n=3
C
Temperature (°C)
Days Post-Infection (d.p.i.)
Male n=22
Female n=8
Sham/PBS n=3
D
Probability of Survival
Days Post-Infection (d.p.i.)
Male n=22
Female n=8
Sham/PBS n=3
E
RNA Copies / mg of tissue
Days Post-Infection (d.p.i.)
Brain
Lung
F
RNA Copies/mL
Days Post-Infection (d.p.i.)

Figure 2

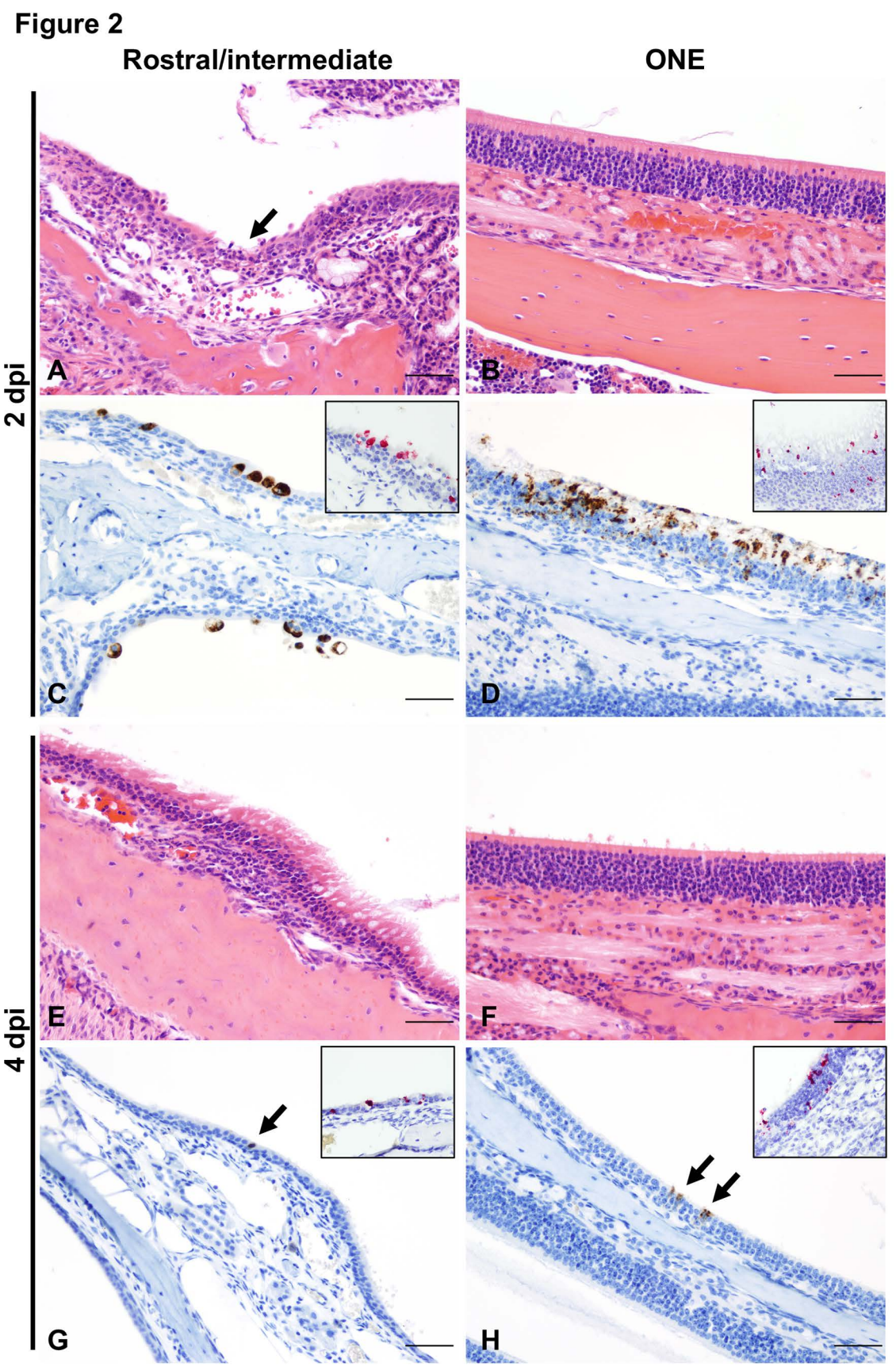

Figure 3

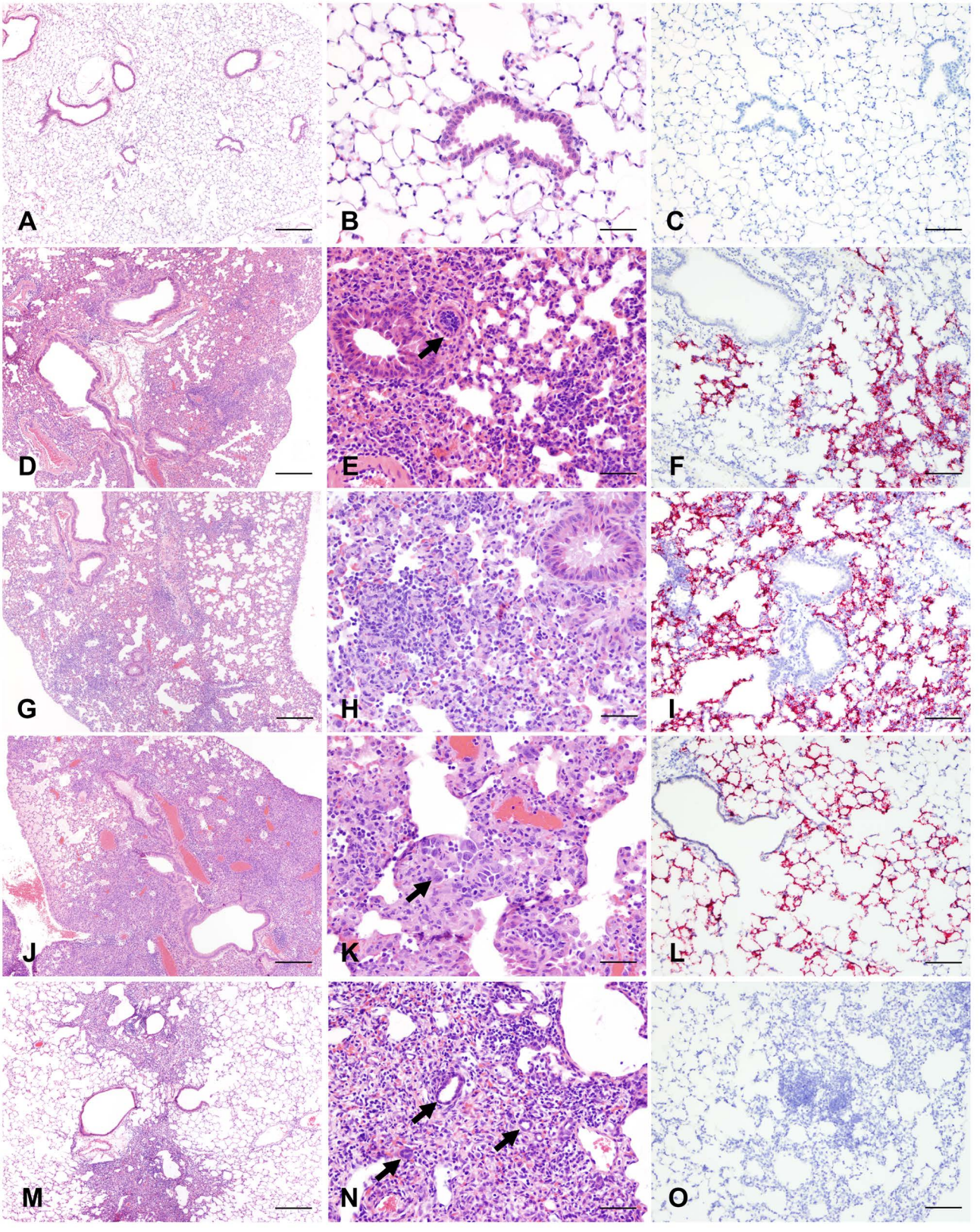

Figure 4

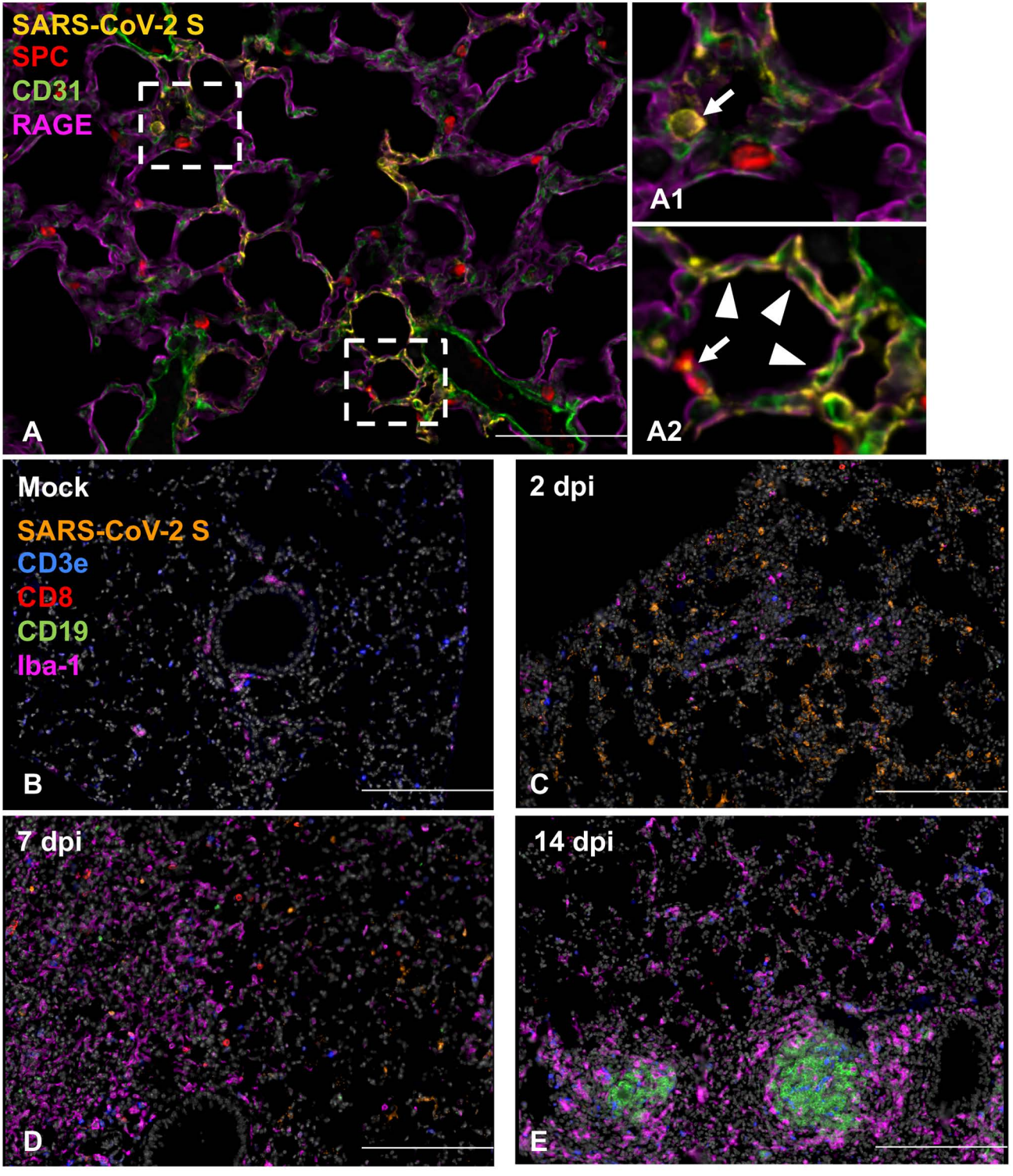
SARS-CoV-2 S
SPC
CD31
RAGE
A
A1
A2
Mock
SARS-CoV-2 S
CD3e
CD8
CD19
Iba-1
B
2 dpi
C
7 dpi
D
14 dpi
E

Figure 5

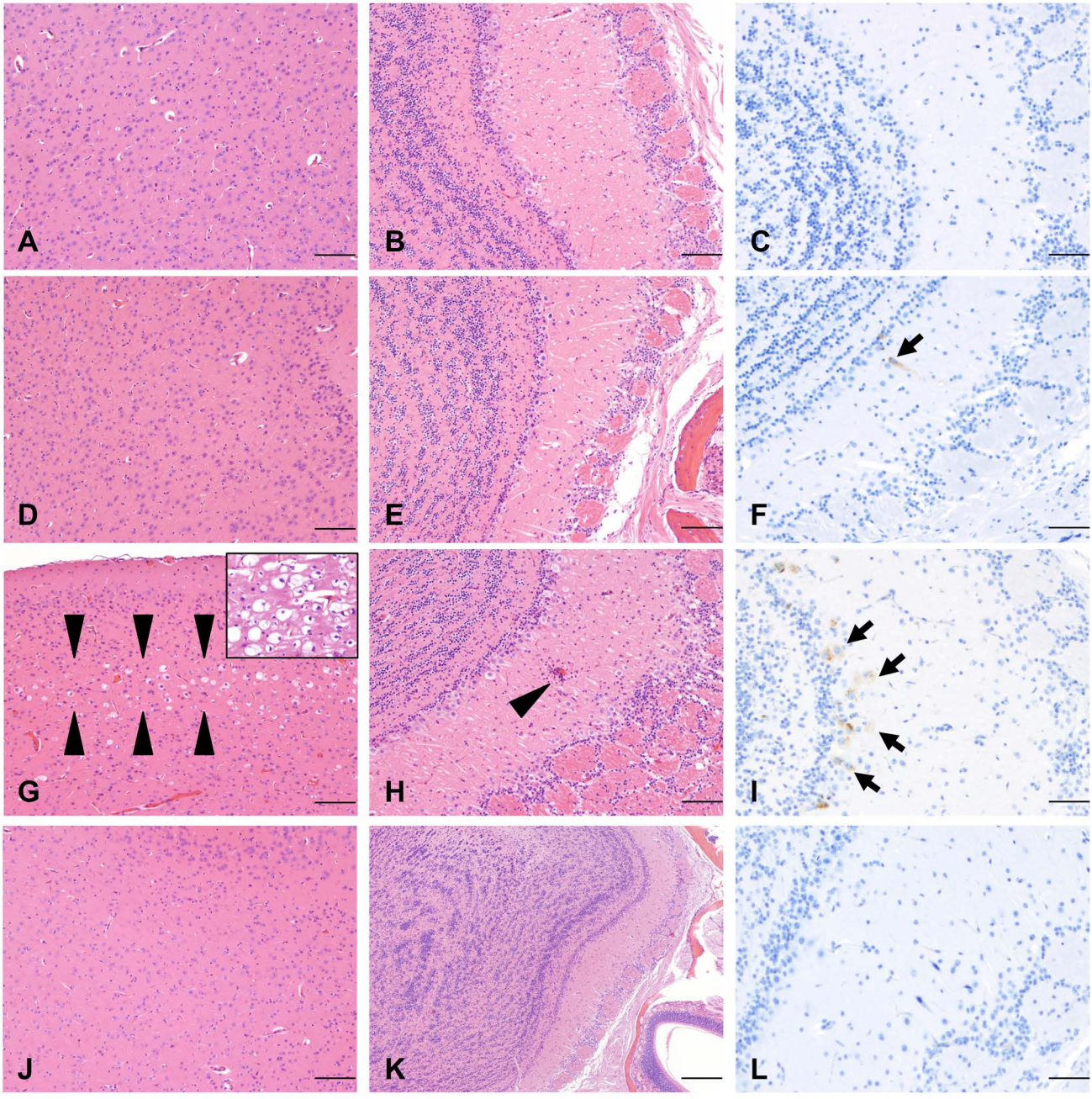

Figure 6

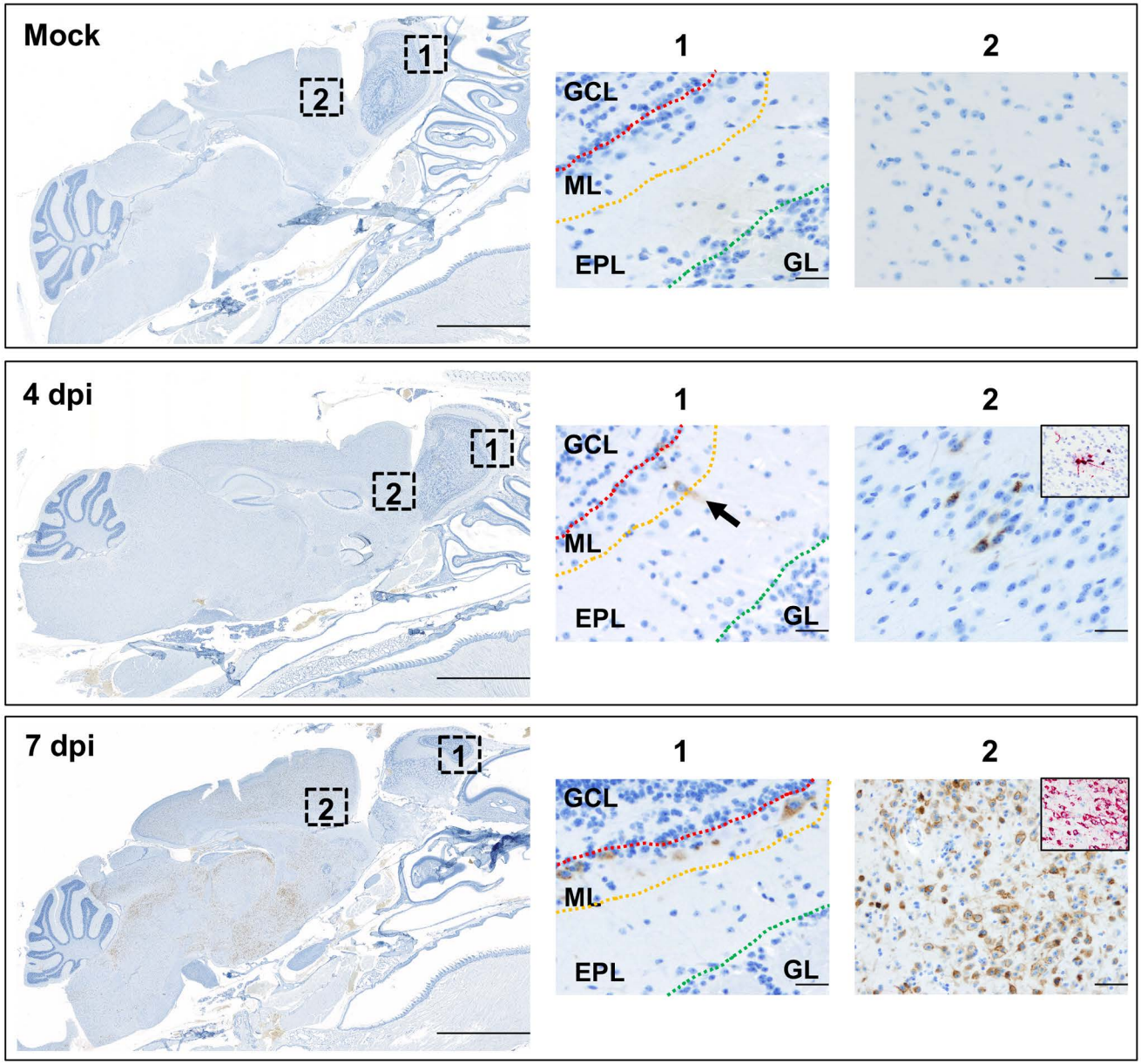
Mock
1
2
1
2
GCL
ML
EPL
GL
4 dpi
1
2
1
2
GCL
ML
EPL
GL
7 dpi
1
2
1
2
GCL
ML
EPL
GL

Figure 7

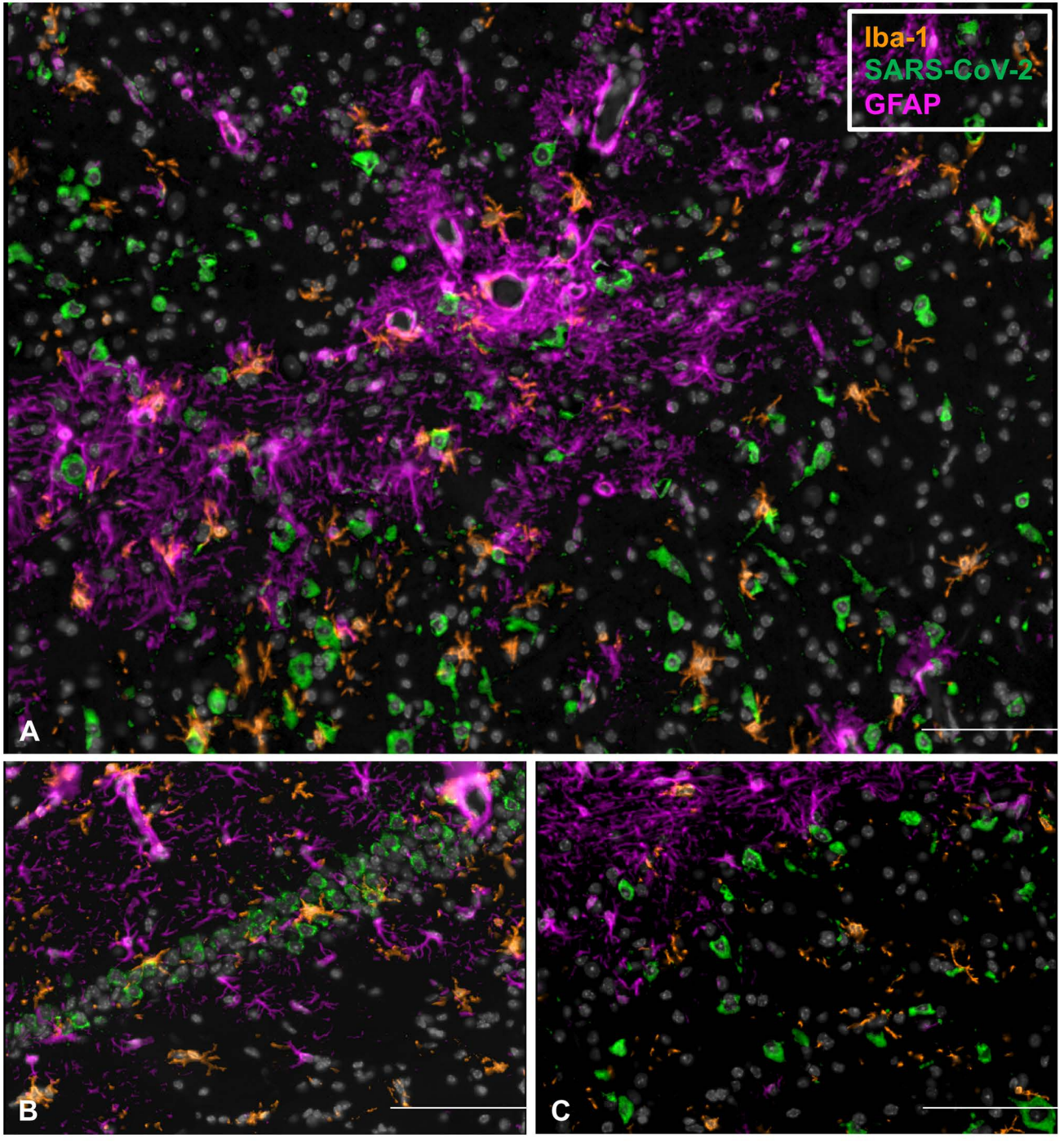

Figure 8

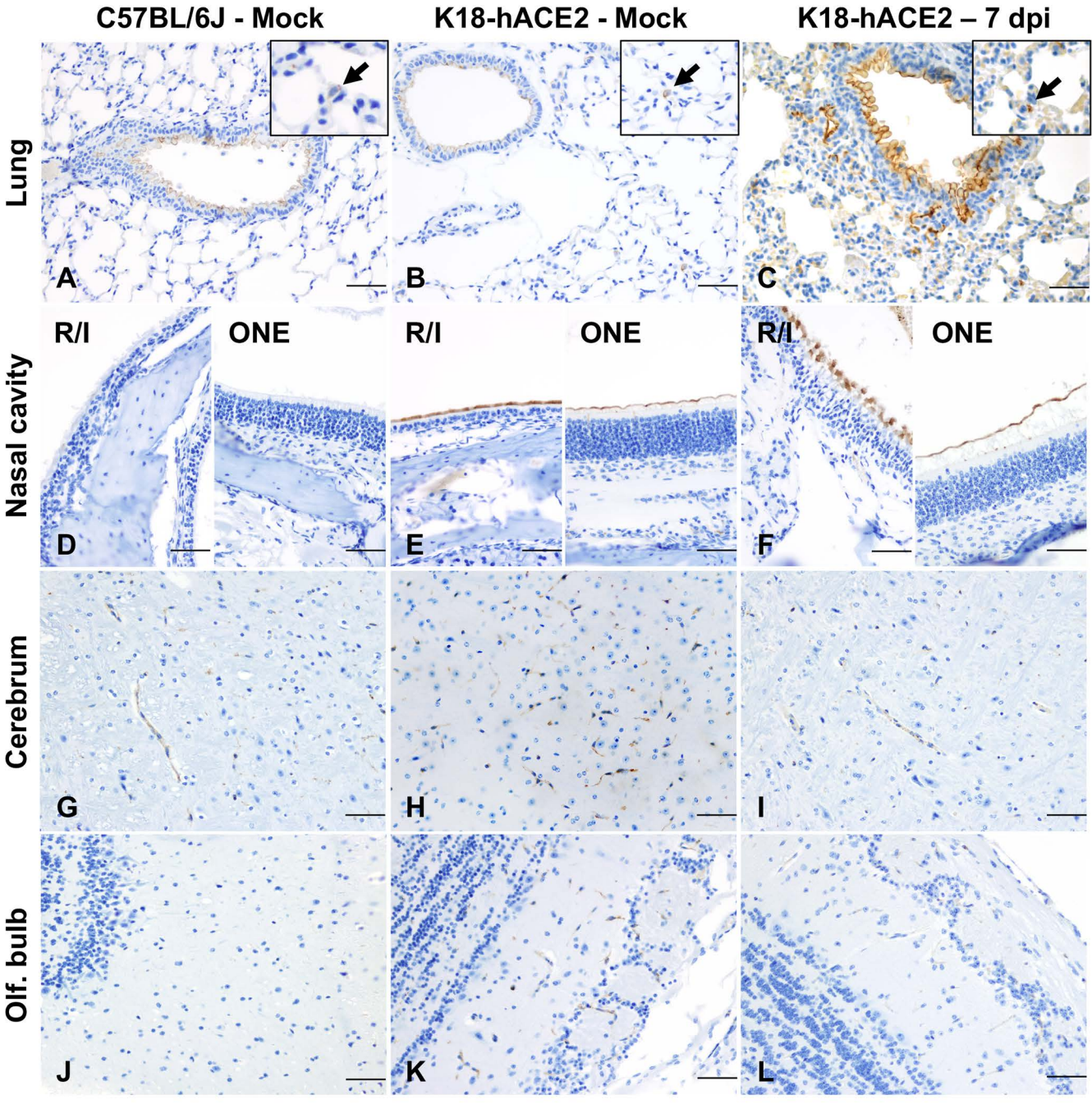
C57BL/6J - Mock
K18-hACE2 - Mock
K18-hACE2 – 7 dpi
Lung
Nasal cavity
Cerebrum
Olf. bulb
A
B
C
R/I
ONE
R/I
ONE
R/I
ONE
D
E
F
G
H
I
J
K
L

Figure 9

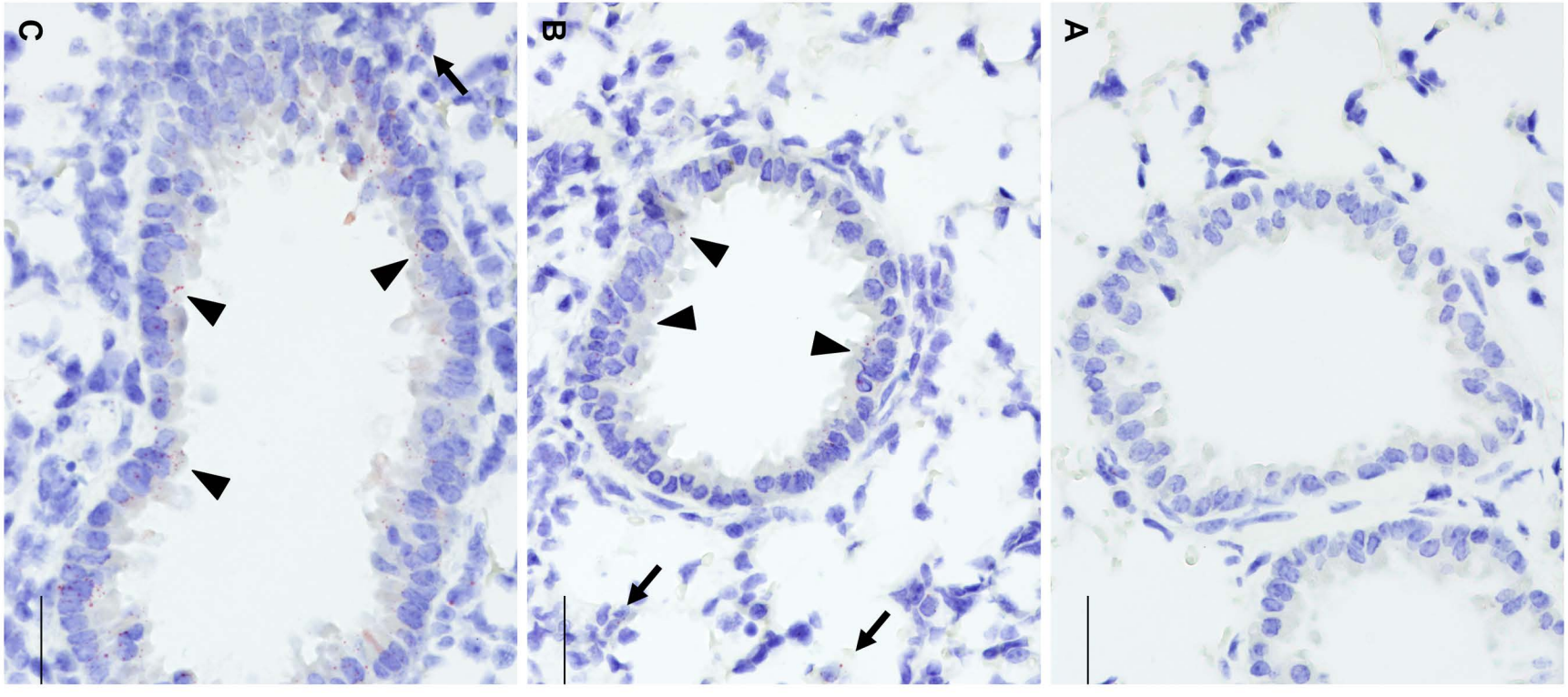

Figure 10